bioRxiv preprint doi: https://doi.org/10.1101/2020.06.08.139592; this version posted June 9, 2020. The copyright holder for this preprint (which was not certified by peer review) is the author/funder, who has granted bioRxiv a license to display the preprint in perpetuity. It is made available under aCC-BY 4.0 International license.

Quantitative fluorescence lifetime imaging uncovers a novel role for KCC2 chloride transport in dendritic microdomains

Nicholas L. Weilinger*[1], Jeffrey M. LeDue[1], Kristopher T. Kahle[2] and Brian A. MacVicar*[1]

Affiliations:

1) Djavad Mowafaghian Centre for Brain Health, University of British Columbia, Vancouver, V6T 1Z3, Canada

2) Departments of Neurosurgery, Pediatrics, and Cellular & Molecular Physiology, Yale School of Medicine, Yale University, New Haven, CT, 06520, USA

*Correspondence: nicholas.weilinger@ubc.ca and bmacvicar@brain.ubc.ca

Keywords: KCC2, Chloride, FLIM, NKCC1, MQAE, swelling, cytotoxic edema, dendrite, blebbing

bioRxiv preprint doi: https://doi.org/10.1101/2020.06.08.139592; this version posted June 9, 2020. The copyright holder for this preprint (which was not certified by peer review) is the author/funder, who has granted bioRxiv a license to display the preprint in perpetuity. It is made available under aCC-BY 4.0 International license.

Abstract

Intracellular chloride ion ($[Cl^-]_i$) homeostasis is critical for synaptic neurotransmission yet variations in subcellular domains are poorly understood owing to difficulties in obtaining quantitative, high-resolution measurements of dendritic $[Cl^-]_i$. We combined whole-cell patch clamp electrophysiology with simultaneous fluorescence lifetime imaging (FLIM) of the Cl^- dye MQAE to quantitatively map dendritic Cl^- levels in normal or pathological conditions. FLIM-based $[Cl^-]_i$ estimates were corroborated by Rubi-GABA uncaging to measured E_{GABA}. Low baseline $[Cl^-]_i$ in dendrites required Cl^- efflux via the K^+-Cl^- cotransporter KCC2 (*SLC12A5*). In contrast, pathological NMDA application generated spatially heterogeneous subdomains of high $[Cl^-]_i$ that created dendritic blebs, a signature of ischemic stroke. These discrete regions of high $[Cl^-]_i$ were caused by reversed KCC2 transport. Therefore monitoring $[Cl^-]_i$ microdomains with a new high resolution FLIM-based technique identified novel roles for KCC2-dependent chloride transport to generate dendritic microdomains with implications for disease.

Introduction

Neuronal function is intrinsically tuned by regulation of the intracellular Cl^- concentration ($[Cl^-]_{i,}$) which is critical for early brain development, setting membrane excitability, and cell volume regulation (Doyon et al., 2016; Kaila et al., 2014; Rungta et al., 2015). In mature nerve cells, low $[Cl^-]_i$ is maintained by K^+-Cl^- cotransporter (KCC2)-dependent extrusion to set gamma aminobutyric acid (GABA)ergic inhibitory tone (Cordero-Erausquin et al., 2005; Kahle et al., 2013; Staley and Proctor, 1999). KCC2 is expressed throughout the dendritic arbor in hippocampal and cortical pyramidal neurons (Gauvain et al., 2011; Gulyas et al., 2001) and is highly expressed in synaptic regions in close proximity to N-methyl-D-aspartate (NMDA), GABA, and α-amino-3-hydroxy-5-methyl-4-isoxazolepropionic acid (AMPA) receptors to shape local excitatory/inhibitory potentials via shunting- and feeback-inhibition, and

bioRxiv preprint doi: https://doi.org/10.1101/2020.06.08.139592; this version posted June 9, 2020. The copyright holder for this preprint (which was not certified by peer review) is the author/funder, who has granted bioRxiv a license to display the preprint in perpetuity. It is made available under aCC-BY 4.0 International license.

ionic plasticity (Chevy et al., 2015; Doyon et al., 2016; Garand et al., 2019; Gauvain et al., 2011). It is becoming clear that $[Cl^-]_i$ heterogeneity in neuronal subdomains is a key determinant of regional neurotransmission [(Barker and Ransom, 1978; Berglund et al., 2006; Glykys et al., 2014; Khirug et al., 2008; Kuner and Augustine, 2000), but also that local perturbations in $[Cl^-]_i$ may underlie synaptic dysfunction. For instance, KCC2 dysregulation has been implicated in multiple neurological disorders that involve synaptodendritic disinhibition, including epilepsy, neuropathic pain, schizophrenia, and autism (Cohen et al., 2002; Coull et al., 2003; Hyde et al., 2011; Steffensen et al., 2015; Tao et al., 2012). However, the spatial distribution and magnitude of dendritic $[Cl^-]_i$ changes in these diseases are poorly understood due to a lack of quantitative imaging of $[Cl^-]_i$ dynamics at the subcellular level.

The dynamic nature of Cl^- homeostasis makes it challenging to study using conventional electrophysiology or imaging techniques. Manipulating $[Cl^-]_i$ by whole-cell patch dialysis is difficult due to compensatory KCC2 or NKCC1 transport to re-establish physiological $[Cl^-]_i$ (Cordero-Erausquin et al., 2005; Doyon et al., 2016). Imaging genetically encoded fluorescent proteins like Clomeleons (Berglund et al., 2006; Grimley et al., 2013; Kuner and Augustine, 2000) and Cl^-/H^+ sensors (Mukhtarov et al., 2013; Sulis Sato et al., 2017) use ratiometric intensity emissions that are marred by divergent light scattering that is wavelength-, tissue depth-, and age-dependent (Oheim et al., 2001). These probes are also sensitive to pH (Arosio et al., 2007; Tsien, 1998), which is problematic given the interrelationship between Cl^- and HCO_3^- cotransport (Kaila, 1994) and their joint permeabilities through many Cl^- channels (Bormann et al., 1987; Jun et al., 2016).

We adopted a Fluorescence Lifetime Imaging (FLIM)-based strategy to circumvent the limitations of ratiometric sensors and establish whether $[Cl^-]_i$ microdomains could be imaged.

bioRxiv preprint doi: https://doi.org/10.1101/2020.06.08.139592; this version posted June 9, 2020. The copyright holder for this preprint (which was not certified by peer review) is the author/funder, who has granted bioRxiv a license to display the preprint in perpetuity. It is made available under aCC-BY 4.0 International license.

FLIM is insensitive to changes in dye concentration, light scattering, and photobleaching (Chen et al., 2013; Lloyd et al., 2010), making it ideal for quantifying $[Cl^-]_i$. The Cl^- sensor N-(ethoxycarbonylmethyl)-6-methoxyquinolinium bromide (MQAE) is suitable for FLIM with a broad dynamic range of lifetimes and is insensitive to pH (Gensch et al., 2015; Kaneko et al., 2002). Bulk-loaded MQAE has been used for quantitative Cl^- imaging *in situ* in Bergmann glia, dorsal root ganglion- and somatosensory neurons (Funk et al., 2008; Gilbert et al., 2007; Untiet et al., 2017), and in large dendritic knobs of the vomeronasal organ (Kaneko et al., 2004; Untiet et al., 2016). However, neurons bulk-loaded with MQAE have poor signal-to-noise over background staining, making it difficult to measure $[Cl^-]_i$ with synaptic resolution.

Here, we explored the utility of combining MQAE-FLIM with whole-cell patch clamp electrophysiology to measure dynamic variations in dendritic $[Cl^-]_i$ and the spatial distributions of these changes under both physiological and pathological conditions. We show MQAE-FLIM can accurately quantify $[Cl^-]_i$ subdomains in dendrites, and that basal $[Cl^-]_i$ is maintained even when experimentally challenged with elevated Cl^- loads. Using MQAE-FLIM, we quantified the relative contributions of KCC2 and NKCC1 in setting regional Cl^- electrochemical gradients, which we corroborated using Rubi-GABA uncaging to calculate E_{GABA} (Rial Verde et al., 2008). Lastly, we demonstrate that NMDA can generate localized dendritic microdomains with regions of remarkably high and persistent dendritic $[Cl^-]_i$ gradients. The formation of dendritic microdomains leads to the appearance of dendritic varicosities ("blebbing") a hallmark of dendritic pathology. Remarkably, bleb formation was prevented by furosemide, indicating localized Cl^- loading was due to reversed K^+/Cl^- transport. Together, our work highlights the advantages of MQAE-FLIM to measure $[Cl^-]_i$ shifts with sub-micrometer resolution that would be otherwise undetectable using intensity imaging or electrophysiology alone. Additionally, we

bioRxiv preprint doi: https://doi.org/10.1101/2020.06.08.139592; this version posted June 9, 2020. The copyright holder for this preprint (which was not certified by peer review) is the author/funder, who has granted bioRxiv a license to display the preprint in perpetuity. It is made available under aCC-BY 4.0 International license.

have identified a novel role for KCC2 in dendritic microdomain Cl^- homeostasis that critically impacts neuronal structure and function.

Results

MQAE-FLIM calibrations for determination of $[Cl^-]_i$

As a first step we determined the reliability of MQAE-FLIM to report $[Cl^-]_i$ by calibrating the dye *in situ* (in bulk-loaded cells) and *in vitro* (in recording solution in sealed pipettes) by time-correlated single-photon counting using 2-photon microscopy (Fig 1a). *In situ* calibrations were conducted in acute brain slices bulk-loaded with MQAE using nigericin and tributyltin to equilibrate $[Cl^-]_i = [Cl^-]_o$ across neuronal membranes (Gensch et al., 2015; Kovalchuk and Garaschuk, 2012). We then measured MQAE-FLIM lifetimes corresponding to various Cl^- concentrations (henceforth *MQAE*-$[Cl^-]_i$, Fig 1b,c) in parallel to intensity changes. Bulk-loaded MQAE intensity decreased significantly in response to increasing $[Cl^-]_o$ but we also observed progressive decline over time due to a combination of dye loss and photobleaching (Fig 1a,c). Indeed, intensity changes did not reverse in $0[Cl^-]_o$ to wash out Cl^- (Fig 1d). In contrast, the MQAE-FLIM channel revealed discrete lifetime changes in response to increasing $[Cl^-]_o$ that fully recovered in $0[Cl^-]_o$ washout despite the reduction in intensity signal (Fig 1d,e), highlighting the advantage and utility of FLIM in overcoming intensity artifacts arising from changes in dye concentration.

To combine MQAE-FLIM with whole-cell patch clamp, we conducted an additional *in vitro* calibration to complement and compare with the bulk-loaded *in situ* calibration. Whole cell

bioRxiv preprint doi: https://doi.org/10.1101/2020.06.08.139592; this version posted June 9, 2020. The copyright holder for this preprint (which was not certified by peer review) is the author/funder, who has granted bioRxiv a license to display the preprint in perpetuity. It is made available under aCC-BY 4.0 International license.

117 loading provided improved signal to noise in dendritic compartments but it was important to
118 calibrate MQAE in the electrode solution that included HEPES and gluconate (Kaneko et al.,
119 2002). MQAE was dissolved in a K-gluconate recording solution with varied Cl^- concentrations,
120 and MQAE-FLIM readouts were measured in sealed, temperature-controlled pipettes. Cl^--
121 dependent MQAE lifetimes varied over a broad dynamic range, from ~4.1 ns to ~1.2 ns when
122 $[Cl^-]_{pipette}$ was increased from 2.5 mM to 110 mM, respectively (Fig 1f-h). The calibration data
123 were well-fit ($R^2 = 0.992$) to a single exponential decay curve with a calculated $K_d = 23.78$ mM
124 $[Cl^-]$ that should be suitable to capture physiological to pathological variations in $[Cl^-]_i$ (Fig 1h).
125 The reciprocal of the dataset from Fig 1h correlated with a linear regression analysis (Fig 1i),
126 confirming that MQAE works through collisional Cl^- quenching and therefore should not buffer
127 Cl^- in solution (Verkman et al., 1989). As expected, the Cl^- sensitivity of MQAE differed in *in*
128 *situ* and *in vitro* calibration environments (Stern-Volmer constants, $K_{SV} = 6.53\ M^{-1}$ and $20.19\ M^{-1}$
129 , respectively, Fig 1j), and the coefficient of variance was significantly lower in the *in vitro*
130 setting (Fig 1k).

131

132

bioRxiv preprint doi: https://doi.org/10.1101/2020.06.08.139592; this version posted June 9, 2020. The copyright holder for this preprint (which was not certified by peer review) is the author/funder, who has granted bioRxiv a license to display the preprint in perpetuity. It is made available under aCC-BY 4.0 International license.

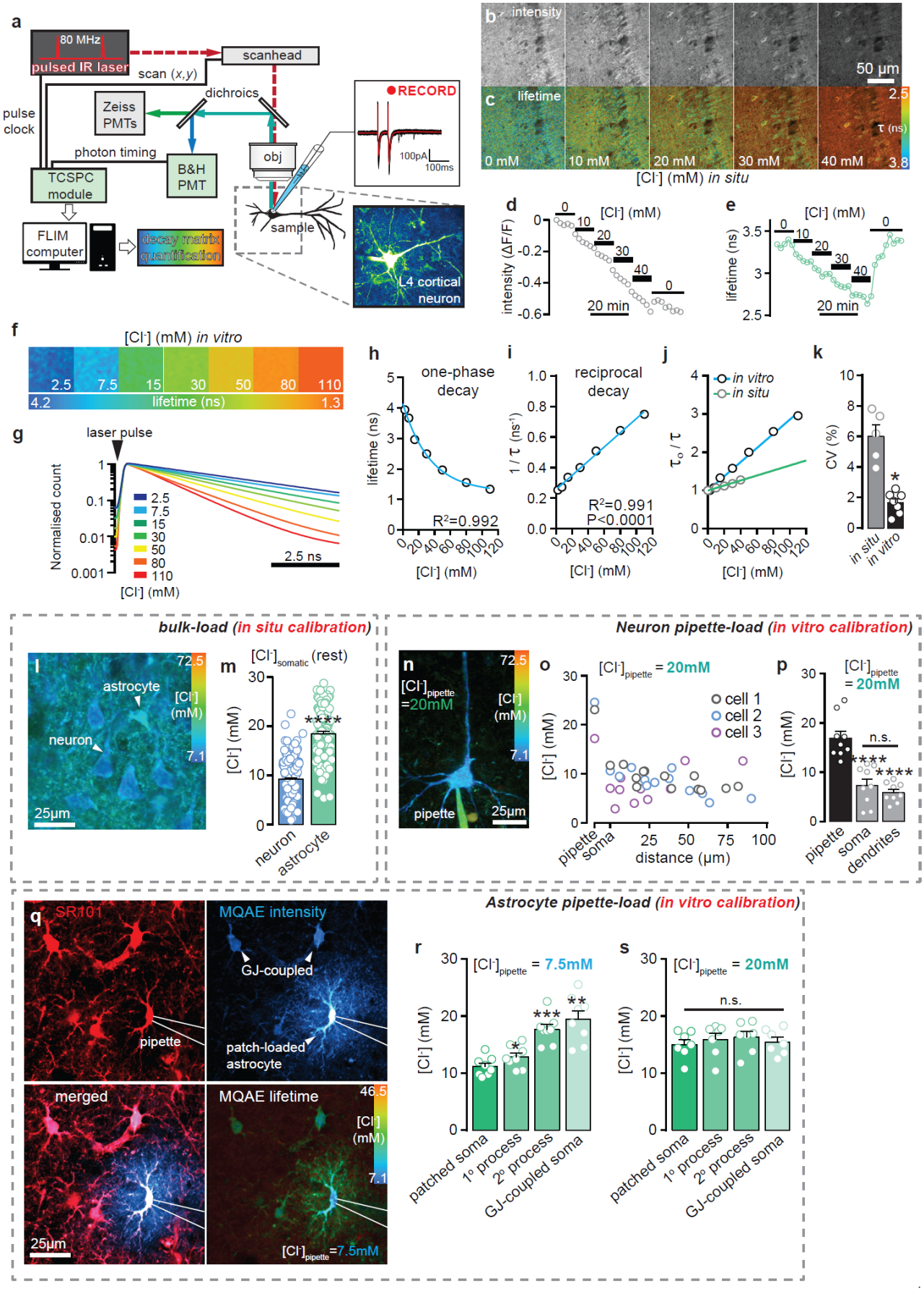

bioRxiv preprint doi: https://doi.org/10.1101/2020.06.08.139592; this version posted June 9, 2020. The copyright holder for this preprint (which was not certified by peer review) is the author/funder, who has granted bioRxiv a license to display the preprint in perpetuity. It is made available under aCC-BY 4.0 International license.

Figure 1. Fluorescence Lifetime Imaging reveals distinct Cl^- handling in neurons and astrocytes. a) Schematic of the time-correlated single photon counting FLIM setup pairing 2P laser imaging system with a Becker & Hickl SPC FLIM module and whole-cell patch clamp electrophysiology. **b)** MQAE-intensity image series of CA1 hippocampal neurons in the presence of nigericin and tributyltin to equilibrate $[Cl^-]_o$:$[Cl^-]_i$ across plasma membranes. $[Cl^-]_o$ was sequentially increased to alter $[Cl^-]_i$ and therefore MQAE-intensity. **c)** MQAE-FLIM readouts from images in 'b'. **d)** Intensity measures from CA1 neuronal somata when $[Cl^-]_o$ is manipulated from 0 to 40 mM. Note that the signal does not reach steady state, nor does it recover to baseline upon washout. **e)** Corresponding MQAE-$[Cl^-]_i$ values for intensity measurements in 'd'. Note that MQAE-FLIM signals reach steady state and that the Cl^- washout is quantifiable. **f)** Example FLIM images of *in vitro* MQAE calibration. **g)** Normalized MQAE lifetime curves at varying $[Cl^-]$. **h)** MQAE-FLIM calibration data fit to a one-phase exponential decay curve consistent with a collisional quenching model. **i)** The reciprocal of the curve in 'd' confirms a linear relationship. **j)** KSV plots comparing calibrations obtained *in vitro* (in bulk-loaded cells) and *in vitro* (in sealed pipettes). **k)** Coefficient of variance (CV) plots comparing *in vitro* and *in situ* calibration data shows that the variability of lifetime readouts is lower *in vitro* ($P<0.05$, student's t-test). **l)** Exemplar image of layer 4 cortical neurons and an astrocyte bulk loaded with MQAE. **m)** Mean somatic $[Cl^-]_i$ measurements with MQAE-FLIM reveal significantly higher basal $[Cl^-]_i$ in astrocytes (n=111 cells) compared to neurons (n=197 cells)(slices=6, ****$P<0.0001$, student's t-test). **n)** Z-projection MQAE-FLIM image of layer 4 pyramidal neuron patch clamped with MQAE (6 mM) and set $[Cl^-]_i$ (20 mM) in the pipette. **o)** Quantification of $[Cl^-]_i$ plotted vs distance from the soma for three example cells to measure the precipitous drop in $[Cl^-]_i$ from the pipette to distal dendrites. **p)** Comparison of average $[Cl^-]_i$ readouts of all cells patched with $[Cl^-]_{pipette}$ = 20 mM (n=9 cells, ****$P<0.0001$, one-way ANOVA with Tukey test). **q)** Astrocytes identified by SR101 staining (top left) were patch clamped and dialysed with MQAE (top right) 7.5 mM Cl^-. MQAE signal was detected in gap-junctionally (GJ) coupled astrocytes. **r)** Average MQAE-FLIM measurements comparing somatic $[Cl^-]_i$ to 1° and 2° processes (*$P = 0.0171$ and ***$P = 0.0002$, respectively), as well as to somatic ROIs from GJ-coupled astrocytes (**$P = 0.0042$) when $[Cl^-]_{pipette}$ = 7.5 mM (n= 8 slices, data compared to patched soma as a control, one-way ANOVA with Tukey test). **s)** Average MQAE-FLIM comparisons when $[Cl^-]_{pipette}$ = 20 mM (n= 7 slices, $P>0.05$, one-way ANOVA with Tukey test).

bioRxiv preprint doi: https://doi.org/10.1101/2020.06.08.139592; this version posted June 9, 2020. The copyright holder for this preprint (which was not certified by peer review) is the author/funder, who has granted bioRxiv a license to display the preprint in perpetuity. It is made available under aCC-BY 4.0 International license.

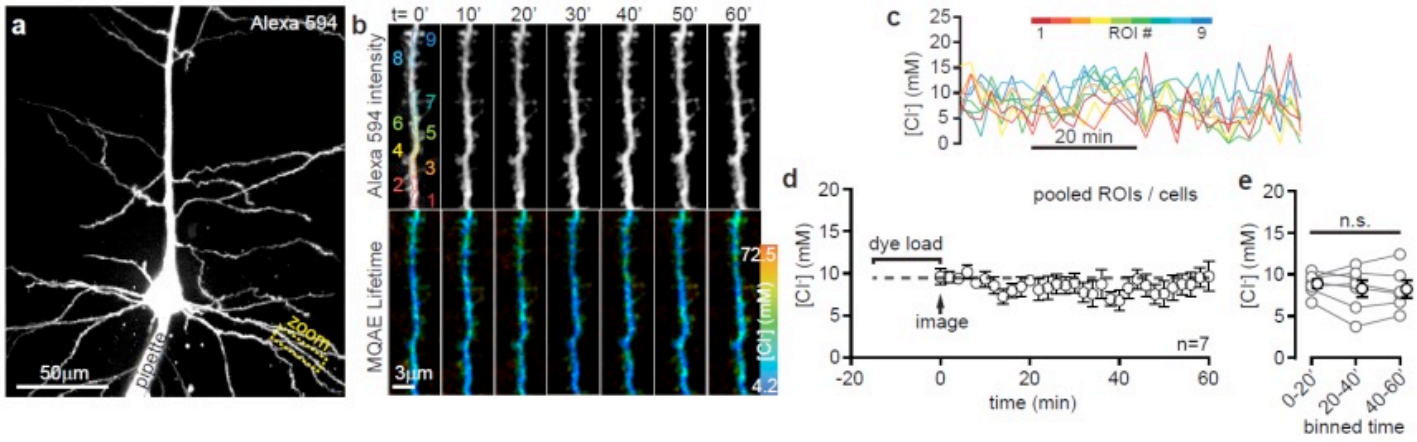

Supplemental Figure 1. *MQAE*-$[Cl^-]_i$ readouts are stable in dendrites. a) Maximum intensity projection z-stack image of a cortical neuron patch-loaded with Alexa594 (presented emission) and MQAE. Dashed yellow box denotes basal dendrite imaged in 'b' and 'c'. **b)** Sample Alexa 594 intensity (top panels) and MQAE-FLIM (bottom panels) image series to monitor dendritic morphology and maintain a stable focal plane for MQAE-FLIM. Intensity channel was used to map ROIs for MQAE-FLIM analysis. **c)** Color-coded MQAE-$[Cl^-]_i$ traces from dendrite in 'b'. **d)** Average dendritic $[Cl^-]_i$ over time following a 15 min dye load period. Dendritic $[Cl^-]_i$ was stable over the course of 60 min imaging sessions (n=7 cells). **e)** Quantification of dendritic $[Cl^-]_i$ in 20 min intervals. No net change in $[Cl^-]_i$ was observed ($P>0.05$, Tukey's test on one-way ANOVA), suggesting the relative impact of changes to the cytosolic microenvironment on MQAE-FLIM are negligible.

bioRxiv preprint doi: https://doi.org/10.1101/2020.06.08.139592; this version posted June 9, 2020. The copyright holder for this preprint (which was not certified by peer review) is the author/funder, who has granted bioRxiv a license to display the preprint in perpetuity. It is made available under aCC-BY 4.0 International license.

189

190 **Bulk- and patch-loaded cells report expected $[Cl^-]_i$ with MQAE-FLIM**

191 Resting $[Cl^-]_i$ is reported to range from 6 mM to 13 mM in mature neurons (Delpire and
192 Staley, 2014; Kuner and Augustine, 2000; Staley and Proctor, 1999). We sought to confirm that
193 MQAE-FLIM measures of neuronal $[Cl^-]_i$ matched basal values reported in these previous
194 studies. In neurons bulk loaded with MQAE, mean resting *MQAE*-$[Cl^-]_i$ was calculated to be
195 9.22±0.3 mM $[Cl^-]_i$ in the soma (perinuclear regions of interest [ROI]s) using *in situ* calibration
196 values (Fig 1l,m). $[Cl^-]_i$ was significantly higher in astrocytes (18.48±0.5 mM) visually
197 identified by cell morphology or by co-staining with SR101 (Fig 1l,m), closely matching
198 measurements in cell culture (Gensch et al., 2015).

199 Next, we dialyzed MQAE by whole-cell patch clamp to compare MQAE-FLIM measures
200 using *in vitro* calibration data in the soma and dendrites. Layer 4/5 cortical neurons were patch
201 clamped with $[Cl^-]_{pipette}$ = 20 mM, a commonly used concentration with Ag/AgCl electrodes, and
202 $[Cl^-]_i$ was measured at several distance intervals distal to the soma (Fig 1n,o). By calculating
203 *MQAE*-$[Cl^-]_i$ with *in vitro* calibration values, we observed that somatic $[Cl^-]_i$ was consistently
204 lower than the 20 mM $[Cl^-]_{pipette}$ and that the lower *MQAE*-$[Cl^-]_i$ readouts were stable throughout
205 the proximal and distal dendrites (Fig 1n,o). Cellular $[Cl^-]_i$ in patched neurons closely matched
206 measures from *in situ* bulk loading experiments (from Fig 1l,m), suggesting both methods
207 accurately report resting $[Cl^-]_i$ levels (Fig 1p). As an important control, dendritic MQAE-FLIM
208 readouts were stable over 1 hr (SFig 1), suggesting *MQAE*-$[Cl^-]_i$ measures are minimally
209 affected by spatiotemporal variations of dye or dialysis of HEPES or gluconate from the pipette.

bioRxiv preprint doi: https://doi.org/10.1101/2020.06.08.139592; this version posted June 9, 2020. The copyright holder for this preprint (which was not certified by peer review) is the author/funder, who has granted bioRxiv a license to display the preprint in perpetuity. It is made available under aCC-BY 4.0 International license.

The precipitous drop from $[Cl^-]_{pipette}$ to somatic $[Cl^-]_i$ could be due to: *(1)* homeostatic Cl^- efflux by K^+-Cl^- cotransport, or *(2)* unpredictable interactions between MQAE and the cytosolic microenvironment. The latter case assumes $[Cl^-]_i$ closely matches $[Cl^-]_{pipette}$ (20 mM) and that the measured *MQAE*-$[Cl^-]_i$ is artifactually altered by nonspecific anion quenching. We explored these possibilities by patch loading MQAE in astrocytes, which do not express KCC2 (Williams et al., 1999) and their $[Cl^-]_i$ is reported to range from 20-40 mM (Gensch et al., 2015; Untiet et al., 2017). Patched astrocytes were dialyzed with a $[Cl^-]_{pipette}$ concentration much lower than our *in situ* measure for astrocyte $[Cl^-]_i$ but closer to neuronal $[Cl^-]_i$ (7.5 mM). If hypothesis *(1)* was correct then homeostatic Cl^- import would increase $[Cl^-]_i$ to ~18 mM (Fig 1l) due to high glial expression of NKCC1 (Su et al., 2002; Untiet et al., 2017). Somatic *MQAE*-$[Cl^-]_i$ in patched astrocytes was higher (11.16±0.6 mM) than $[Cl^-]_{pipette}$, consistent with the observation that astrocytes maintain a higher $[Cl^-]_i$ than neurons (Fig 1q,r)(Kettenmann and Schachner, 1985; MacVicar et al., 1989; Untiet et al., 2017). Distal measures revealed a progressive increase in $[Cl^-]_i$ in large primary- (1^o) to smaller secondary (2^o) processes of patched astrocytes, with peak measures from astrocyte somata coupled via gap-junctions (GJ)(19.46±1.46 mM, Fig 1r). In contrast, we observed a slight but reliable decrease in $[Cl^-]_i$ across all ROIs (Fig 1s) in astrocytes loaded with $[Cl^-]_{pipette}$ = 20 mM, consistent with an homeostatic decrease by KCC3 (Cordero-Erausquin et al., 2005; Doyon et al., 2016).

Mapping subcellular KCC2 Cl^- export during intracellular Cl^- challenge

The extent of homeostatic Cl^- export via KCC2 was quantified using MQAE-FLIM by applying the inhibitor furosemide in neurons that were dialyzed with a high Cl^- load via the patch pipette ($[Cl^-]_{pipette}$ = 80 mM, normal aCSF $[Cl^-]_o$ = 136 mM). Under these conditions *MQAE*-$[Cl^-]_i$ was stable (somatic change = 2.74 ± 1.25 mM) after 15 min of dye loading (Fig

bioRxiv preprint doi: https://doi.org/10.1101/2020.06.08.139592; this version posted June 9, 2020. The copyright holder for this preprint (which was not certified by peer review) is the author/funder, who has granted bioRxiv a license to display the preprint in perpetuity. It is made available under aCC-BY 4.0 International license.

2ab), suggesting that MQAE diffusion was in stable equilibrium and that its lifetime is not appreciably impacted by hydrolysis (Koncz and Daugirdas, 1994). We again observed a marked decrease in somatic *MQAE*-$[Cl^-]_i$ compared to *MQAE*-$[Cl^-]_{pipette}$ (Fig 3ac) with gradual, distance-dependent reductions in dendrites suggesting substantial Cl^- efflux throughout the dendritic tree. Bath application of furosemide (200 μM) significantly increased dendritic $[Cl^-]_i$ at binned ROIs equidistant to the soma (Fig 2c-e), indicating that the low dendritic $[Cl^-]_i$ required KCC2. Applying furosemide together with picrotoxin to inhibit $GABA_A$-receptors similarly increased $[Cl^-]_i$ by blocking tonic Cl^- efflux from $GABA_AR$ when E_{Cl^-} is depolarized from holding potential (V_m= -60 mV) (Fig 2d,e). Interestingly, $[Cl^-]_i$ was significantly lower in 2° versus 1° dendrites (Fig 2f), consistent with the observation that KCC2 is evenly distributed in dendrites and therefore Cl^- handling should be more efficient where the surface area to volume ratio is high (Doyon et al., 2011). These data suggest neurons defend their Cl^- gradients by KCC2-transport.

KCC2 transport activity is highly regulated by kinase-dependent phosphorylation via the With No-Lysine (K) (WNK) and Ste20p-related Proline Alanine-rich Kinases (SPAK) (Alessi et al., 2014). Phosphorylation or dephosphorylation of threonines (T) T906 and T1007 on the KCC2 c-terminus cause transporter hypo- or hyperfunction, respectively (Friedel et al., 2015; Kahle et al., 2013; Rinehart et al., 2009). To further explore KCC2's role in establishing Cl^- gradients, we repeated the above experiments in knock-in mice in which T906 and T1007 were mutated to alanine (A) (i.e., T906A and T1007A, henceforth "$KCC2^{A/A}$") to mimic KCC2 dephosphorylation and constitutive activation (Friedel et al., 2015; Heubl et al., 2017; Moore et al., 2018; Pisella et al., 2019; Watanabe et al., 2019). We observed a sharp drop in somato-dendritic *MQAE*-$[Cl^-]_i$ in patched $KCC2^{A/A}$ neurons compared to wild-type controls ($KCC2^{WT}$),

bioRxiv preprint doi: https://doi.org/10.1101/2020.06.08.139592; this version posted June 9, 2020. The copyright holder for this preprint (which was not certified by peer review) is the author/funder, who has granted bioRxiv a license to display the preprint in perpetuity. It is made available under aCC-BY 4.0 International license.

consistent with an increased pump capacity of $KCC2^{A/A}$ (Fig 2g). Additionally, we found no difference in equidistant $[Cl^-]_i$ measures between pyramidal neurons in brain slices from control rat versus mouse ($KCC2^{WT}$) (control and $KCC2^{WT}$ groups from Fig 2e,g, respectively, $P>0.05$ by two-way ANOVA). This similarity suggests that the KCC2 extrusion capacity is consistent between these species. We conclude that MQAE-FLIM can detect dynamic fluctuations in $[Cl^-]_i$ through manipulation of KCC2 activity, and that discrepancy between *MQAE*-$[Cl^-]_i$ and *MQAE*-$[Cl^-]_{pipette}$ is primarily due to homeostatic Cl^- extrusion.

If the *MQAE*-$[Cl^-]_{pipette}$:*MQAE*-$[Cl^-]_i$ mismatch was due to the cytosolic environment, somatic $[Cl^-]_i$ readouts from Fig 2 would be closer to 80 mM instead of the recorded ~30-40 mM, and true $[Cl^-]_i$ would be close to a ceiling and likely not amenable to increase. We tested whether *MQAE*-$[Cl^-]_i$ in these conditions could be increased to match $[Cl^-]_{pipette}$ by experimentally inhibiting Cl^- fluxes. Neurons were voltage clamped at the calculated E_{Cl^-} for $[Cl^-]_{pipette}$ = 80 mM (E_{Cl^-} = -14 mV), and a cocktail of blockers was applied to inhibit Cl^- fluxes, including: picrotoxin ($GABA_AR$), furosemide, bumetanide (NKCC1), niflumic acid (NFA, Ca^{2+}-activated Cl^- channels), and 5-Nitro-2-(3-phenylpropylamino)benzoic acid (NPPB, VRACs). Under these conditions, somatic $[Cl^-]_i$ steadily increased from 36.83±2.1 mM at break-in to a plateau of 64.11±1.8 mM over 20 min (Fig 3a-c). This was accompanied by a volume increase (as evidenced by the increase in mean cross sectional area = 34.8%, Fig 3a,b,d) because Cl^- loading is a key driver of swelling (Rothman, 1985; Rungta et al., 2015). Together, these data refute hypothesis *(2)* and suggest that *MQAE*-$[Cl^-]_i$ readouts can be used to quantify Cl^-dynamics via transporter export and efflux through Cl^- channels.

bioRxiv preprint doi: https://doi.org/10.1101/2020.06.08.139592; this version posted June 9, 2020. The copyright holder for this preprint (which was not certified by peer review) is the author/funder, who has granted bioRxiv a license to display the preprint in perpetuity. It is made available under aCC-BY 4.0 International license.

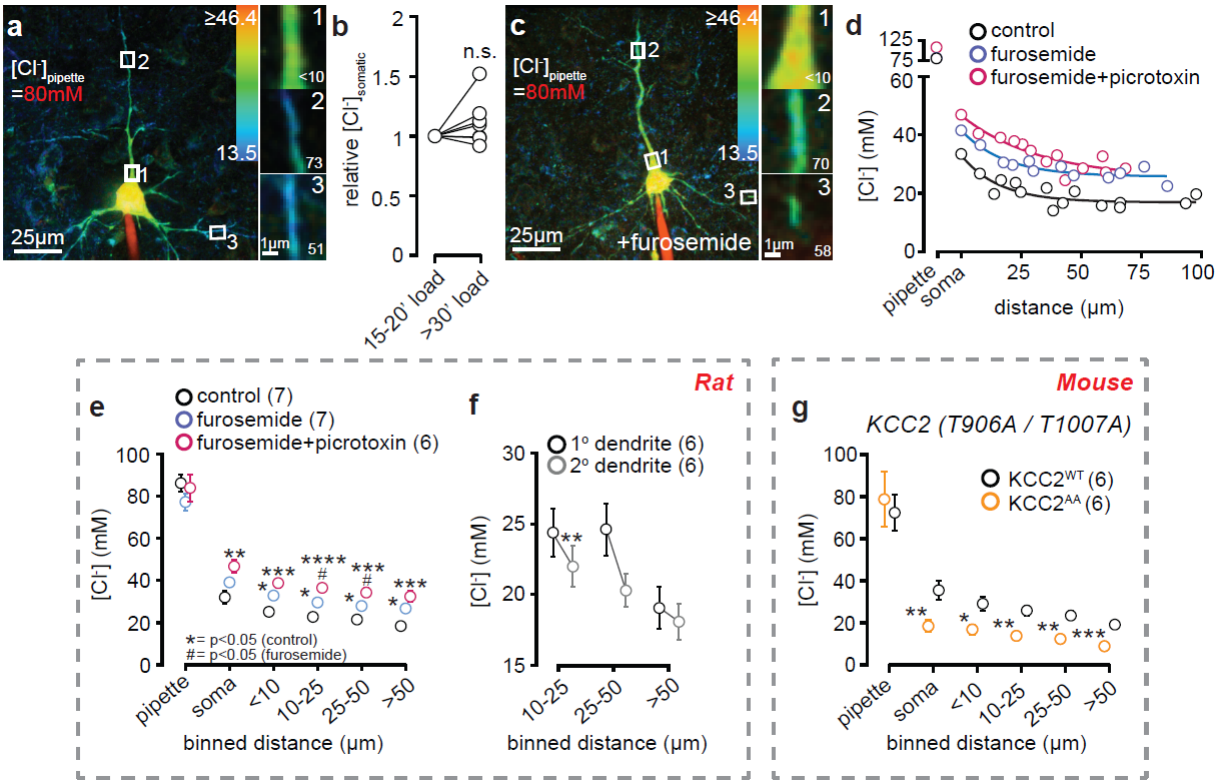

Figure 2. KCC2-dependent Cl^- extrusion during high $[Cl^-]_i$ challenge. a) Left panel: example maximum intensity projection (collapsed Z-stack) image of layer 4 neuron patch filled with $[Cl^-]_{pipette}$ = 80 mM, normal ASF $[Cl^-]_o$ = 136 mM, voltage clamped at -60 mV. Right panels: zoomed ROIs from primary (panels 1&2) and secondary (panel 3) dendrites at different distances from the soma (in µm, bottom right values in figure panels). **b)** Quantification of average $[Cl^-]_i$ measures over time (each point represents whole-cell averages). $[Cl^-]_i$ stabilized after 15 min post whole-cell break-in, and MQAE-FLIM readouts did not change 30 min post break-in. **c)** Exemplar cell loaded with $[Cl^-]_{pipette}$ = 80 mM in the presence of KCC2 blocker furosemide (200 µM), normal ASF $[Cl^-]_o$ = 136 mM, voltage clamped at -60 mV. Zoom panels show higher steady-state $[Cl^-]_i$ measured by MQAE-FLIM compared to 'a', suggesting a KCC2-dependent Cl^- efflux pathway. **d)** Plots of $[Cl^-]_i$ at varying distances from the soma. Application of furosemide alone, or furosemide+picrotoxin (100 µM) increased steady state $[Cl^-]_i$ measures by MQAE-FLIM compared to control. **e)** Quantitative summary comparing drug treatments on $[Cl^-]_i$ at respective distances (*P<0.05 compared to control, $^{\#}$P<0.05 compared to furosemide). **f)** Comparison of $[Cl^-]_i$ between primary and secondary dendrites at binned ROIs equidistant from the soma. $[Cl^-]_i$ measures were relatively lower in 2° vs 1° dendrites at distances of 10-25 µm (**P = 0.0062) from the soma, but not at distances 25-50 µm (P = 0.0517) and >50 µm (P = 0.2467), two-tailed paired t-tests. **g)** Quantitative analysis of $[Cl^-]_i$ by MQAE-FLIM in $KCC2^{A/A}$ mice compared to WT controls patch loaded with $[Cl^-]_{pipette}$ = 80 mM, normal ASF $[Cl^-]_o$ = 136 mM, voltage clamped at -60 mV. $[Cl^-]_i$ was significantly lower in $KCC2^{A/A}$ neurons compared to $KCC2^{WT}$ (from left to right, P = 0.0082, 0.0161, 0.0014, 0.0012, 0.0006), consistent with an increased extrusion capacity of KCC2.

bioRxiv preprint doi: https://doi.org/10.1101/2020.06.08.139592; this version posted June 9, 2020. The copyright holder for this preprint (which was not certified by peer review) is the author/funder, who has granted bioRxiv a license to display the preprint in perpetuity. It is made available under aCC-BY 4.0 International license.

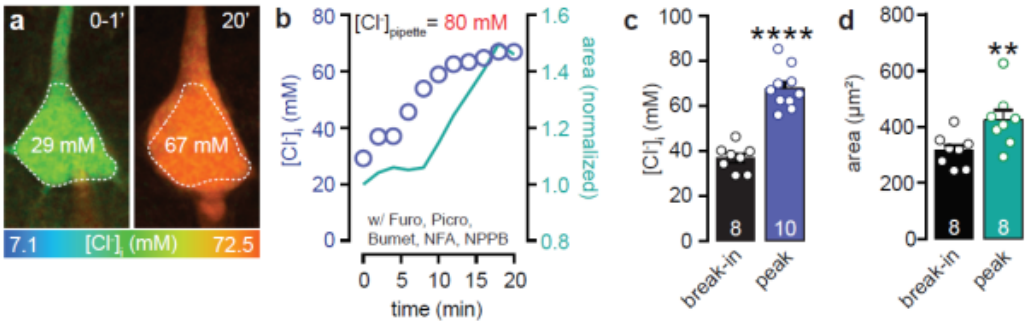

Figure 3. Inhibiting putative routes of Cl^- efflux leads to dramatic increase in $[Cl^-]_i$. a) Example MQAE-FLIM images at whole-cell break in (left panel) and 20 min after (right panel) of cell patch clamped with $[Cl^-]_{pipette}$ = 80 mM, normal ASF $[Cl^-]_o$ = 136 mM, voltage clamped at -14 mV. Experiment performed with furosemide (200 µM), picrotoxin (100 µM) bumetanide (50 µM), NFA (100 µM), and NPPB (100 µM) in the ACSF. **b)** Quantification of somatic $[Cl^-]_i$ and cross-sectional area over time in 'a'. **c)** Summary of peak $[Cl^-]_i$ measures by MQAE compared to whole-cell break-in (0-1 min)(****P<0.0001, two-tailed paired t-test). **d)** Comparison of somatic swelling as measured by cross-sectional area (**P = 0.0018, two-tailed paired t-test).

Local GABA uncaging corroborates MQAE lifetime

As final confirmation that MQAE-FLIM is accurate, we compared spatially coupled FLIM readouts to E_{GABA} measured by local two-photon of uncaging Rubi-GABA (Rial Verde et al., 2008). Rubi-GABA (0.5 mM) was locally applied and photolyzed adjacent to the somatic MQAE-FLIM ROI. In this way we would achieve reasonable voltage clamp in the soma with minimal space clamp artifacts (Fig 4a) (Williams and Mitchell, 2008). These experiments were performed in the absence of the intracellular K^+-channel blocker Cs^+ to prevent perturbation of KCC2 function (Blaesse et al., 2009; Williams and Payne, 2004). In neurons patched with $[Cl^-]_{pipette}$= 80 mM, Rubi-GABA was uncaged at -80 mV to +20 mV and $[Cl^-]_i$ was calculated from

bioRxiv preprint doi: https://doi.org/10.1101/2020.06.08.139592; this version posted June 9, 2020. The copyright holder for this preprint (which was not certified by peer review) is the author/funder, who has granted bioRxiv a license to display the preprint in perpetuity. It is made available under aCC-BY 4.0 International license.

326 E_{GABA} (E_{GABA}-$[Cl^-]_i$, Fig 4b-d). E_{GABA}-$[Cl^-]_i$ and *MQAE*-$[Cl^-]_i$ values were well correlated (Fig 4f)
327 despite known confounds for E_{GABA} measures such as permeability to HCO_3^- (Kaila and Voipio,
328 1987; Kaila et al., 1993). To test the impact Br^- efflux (dissociated from MQAE-Br salt) on
329 E_{GABA}, we reduced the concentration of MQAE 10-fold and found no statistical difference from 6
330 mM MQAE (Fig 4e).

331

332

333

334

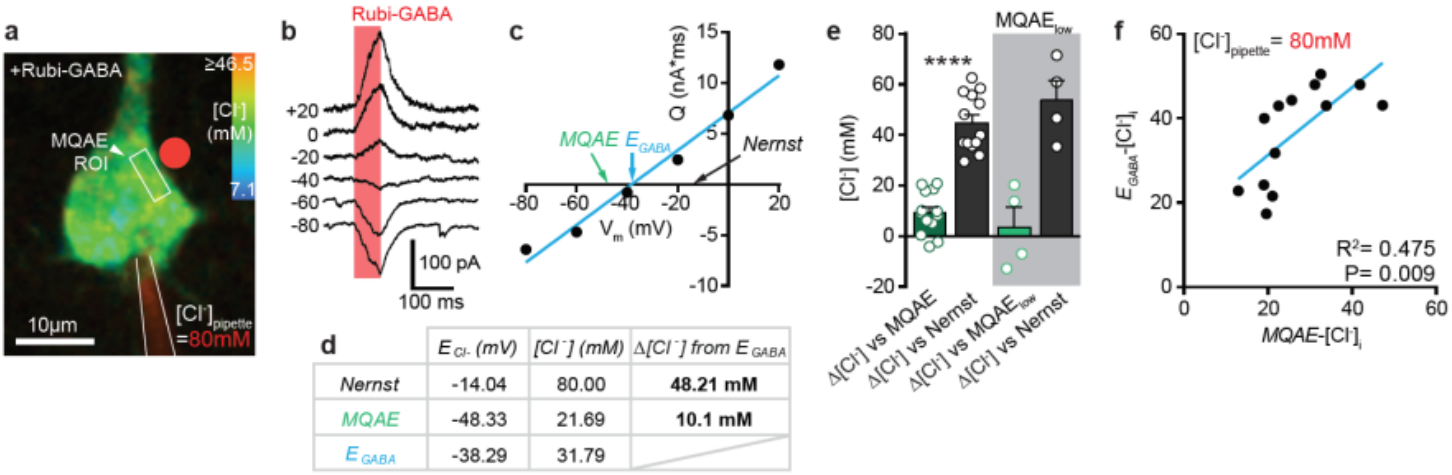

d

	E_{Cl^-} (mV)	$[Cl^-]$ (mM)	$\Delta[Cl^-]$ from E_{GABA}
Nernst	-14.04	80.00	**48.21 mM**
MQAE	-48.33	21.69	**10.1 mM**
E_{GABA}	-38.29	31.79	

335 **Figure 4. Comparison of MQAE-$[Cl^-]_i$ to E_{GABA}-$[Cl^-]_i$. a)** Example image of layer 4 neuron
336 patch-loaded with $[Cl^-]_{pipette}$ = 80 mM, normal ASF $[Cl^-]_o$ = 136 mM. Rubi-GABA was locally
337 applied (0.5 mM) by puff electrode and photolyzed adjacent to the soma (red dot) by 2P-
338 uncaging. **b)** Example whole-cell currents induced by Rubi-GABA uncaging (red box) at
339 different holding potentials. **c)** Charge (Q) and membrane voltage (V_m) plot of Rubi-GABA
340 responses. EGABA is graphically compared to Cl^- reversal calculated by MQAE measurement,
341 as well the E_{Cl^-} estimation that assumes $[Cl^-]_i = [Cl^-]_{pipette}$ (80 mM). **d)** Tabular results from
342 exemplar experiment 'a-c' showing the calculated values for E_{Cl^-} based on the pipette solution
343 (Nernst), the MQAE-FLIM measurement, and the E_{GABA} measurement; the respective predicted
344 $[Cl^-]_i$ values; and the differences in the predicted $[Cl^-]_i$. **e)** Comparison of $[Cl^-]_i$ predicted by
345 E_{GABA} to *MQAE*-$[Cl^-]_i$ and Nernst, ****P<0.0001. **f)** Correlation plot between calculated E_{GABA}-
346 $[Cl^-]_i$ and *MQAE*-$[Cl^-]_i$ values.

bioRxiv preprint doi: https://doi.org/10.1101/2020.06.08.139592; this version posted June 9, 2020. The copyright holder for this preprint (which was not certified by peer review) is the author/funder, who has granted bioRxiv a license to display the preprint in perpetuity. It is made available under aCC-BY 4.0 International license.

Mapping KCC2/NKCC1-dependent control of dendritic Cl^- gradients

We measured the basal contributions of NKCC1 and KCC2 in setting dendritic $[Cl^-]_i$. Proximal basal dendrites ($[Cl^-]_{pipette}$ = 7.5 mM) were imaged by MQAE-FLIM before and after bath application of furosemide or the NKCC1 inhibitor bumetanide (Fig 5a-d). Quantitative and reversible increases in *MQAE*-$[Cl^-]_i$ were observed in furosemide, consistent with disruption of basal Cl^- efflux by KCC2 (Fig 5a-c). On the other hand, bath application of bumetanide (50 µM) to selectively block NKCC1 decreased resting $[Cl^-]_i$ due to reduced Cl^- import. As a positive control, membrane depolarization to +30 mV also increased $[Cl^-]_i$ in the presence of furosemide or bumetanide (Fig 5c,d) but also in the absence of either blocker (Fig 5e), consistent with an increased driving force for Cl^- entry through tonic $GABA_AR$ activity and voltage-activated Cl^- channels. Thus, MQAE-FLIM has the sensitivity to measure millimolar contributions of Cl^- channels and transporters, as well as dynamic $[Cl^-]_i$ changes.

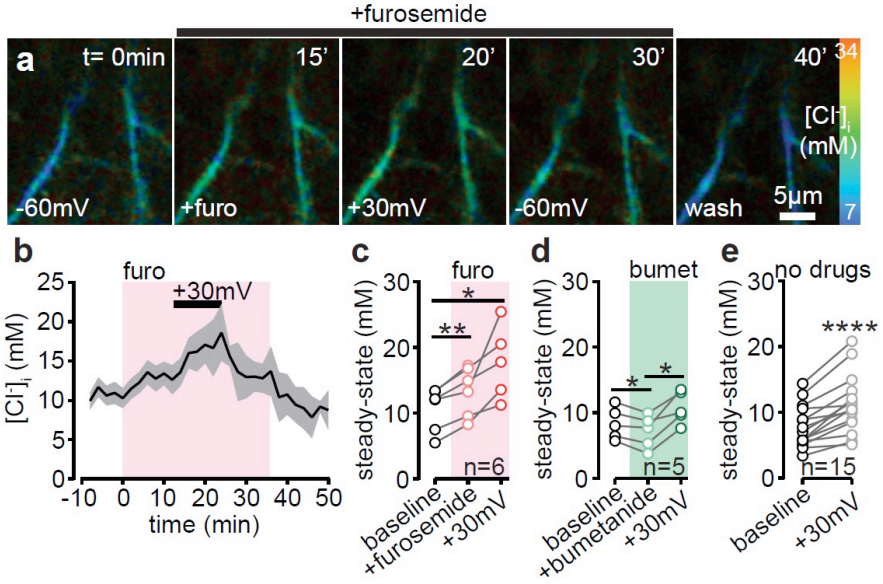

bioRxiv preprint doi: https://doi.org/10.1101/2020.06.08.139592; this version posted June 9, 2020. The copyright holder for this preprint (which was not certified by peer review) is the author/funder, who has granted bioRxiv a license to display the preprint in perpetuity. It is made available under aCC-BY 4.0 International license.

Figure 5. MQAE-FLIM can detect KCC2-dependent changes in $[Cl^-]_i$ with millimolar precision. a) Example MQAE-FLIM image series of $[Cl^-]_i$ in a basal dendrite from a patch clamped layer 4 cortical neuron ($[Cl^-]_{pipette}$ = 7.5 mM) in the presence of furosemide (furo, 200 µM) and membrane depolarization (+30 mV). **b)** Average trace of $[Cl^-]_i$ changes over time in response to furosemide application (pink box) and membrane depolarization (n=6). **c)** Quantitative analysis comparing paired $[Cl^-]_i$ measurements before and after furosemide (**P = 0.006) and membrane depolarization to +30 mV (*P = 0.0378), one-way ANOVA with Tukey test. **d)** Quantitative comparison of paired $[Cl^-]_i$ measurements before and after bumetanide (bumet, 50 µM, *P = 0.026) and membrane depolarization to +30 mV (*P = 0.0165), one-way ANOVA with Tukey test. **e)** Membrane depolarization alone is sufficient to increase dendritic $[Cl^-]_i$, ****P<0.0001, two tailed paired t-test.

MQAE-FLIM reveals heterogeneous Cl^- microdomains in cytotoxic edema

The importance of Cl^- loading in cytotoxic swelling is well established (Rothman, 1985; Rungta et al., 2015) although little is known about the spatiotemporal dynamics and regulation of subcellular Cl^- loading in dendritic regions during edema. Excitotoxic injury in ischemia is thought to be triggered by NMDA receptor overstimulation leading to dendritic swelling and blebbing (Murphy et al., 2008; Thompson et al., 2008; Weilinger et al., 2016; Weilinger et al., 2012). We used MQAE-FLIM to monitor $[Cl^-]_i$ dynamics under intense NMDA receptor stimulation in dendrites to recapitulate this form of ischemic injury. We used a strategy that we previously developed to restrict the actions of bath applied NMDA to only single patched clamped neuron (Dissing-Olesen et al., 2014). In these experiments 6 mM Mg^{2+} was included in the aCSF perfusate to block tissue-wide NMDAR responses from bath applied NMDA. Only single L4/5 cortical neurons that were patch clamped and depolarized to +30 mV to relieve the NMDAR Mg^{2+} block responded to NMDA application (20 µM) (Dissing-Olesen et al., 2014). In this way, swelling was restricted to the patched neuron throughout the experimental time course,

bioRxiv preprint doi: https://doi.org/10.1101/2020.06.08.139592; this version posted June 9, 2020. The copyright holder for this preprint (which was not certified by peer review) is the author/funder, who has granted bioRxiv a license to display the preprint in perpetuity. It is made available under aCC-BY 4.0 International license.

thereby providing the stability to simultaneous track *MQAE*-$[Cl^-]_i$ and morphological changes in dendritic regions over time in the intact brain slice.

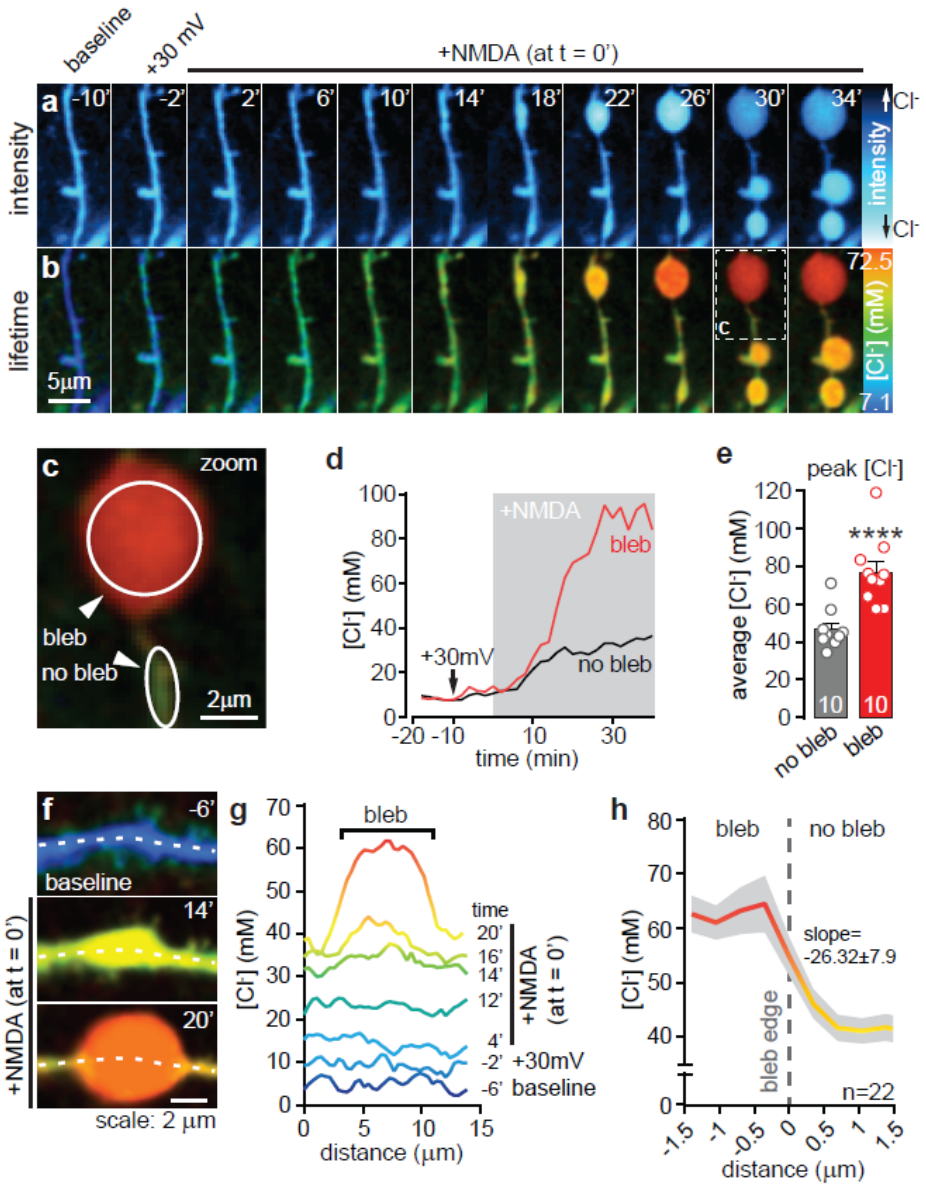

Figure 6. MQAE-FLIM reveals heterogeneous $[Cl^-]_i$ landscapes in excitotoxicity. a) Example imaging time series of MQAE intensity in dendrite from a patch-clamped neuron ($[Cl^-]_{pipette}$ = 7.5 mM) before and after membrane depolarization and bath application of NMDA (20 µM). **b)** MQAE-FLIM image data (same dendrite from 'a') reveals dramatic $[Cl^-]_i$ heterogeneities during dendritic blebbing that are not resolved from intensity images. **c)** Zoomed image of dendrite from 'b' (white box t= 30 min) depicting example ROIs encompassing blebbed

bioRxiv preprint doi: https://doi.org/10.1101/2020.06.08.139592; this version posted June 9, 2020. The copyright holder for this preprint (which was not certified by peer review) is the author/funder, who has granted bioRxiv a license to display the preprint in perpetuity. It is made available under aCC-BY 4.0 International license.

and adjacent un-blebbed dendrite. **d)** Representative $[Cl^-]_i$ measurements over time from bleb and no bleb ROIs in the presence of NMDA. **e)** Quantitative summary of peak $[Cl^-]_i$ measures comparing MQAE-FLIM signal from blebbed and unblebbed ROIs, ****P<0.0001. **f)** MQAE-FLIM time course showing the formation of a bleb. Time (in min) in the top right corner of the images indicates the time relative to application of NMDA (at t = 0 min). Dotted white line indicates the ROI used to measure the pixel-to-pixel $[Cl^-]_i$ levels over distance reported in 'g'. **g)** Spatial $[Cl^-]_i$ readouts from before, during, and after formation of the bleb shown in 'f'. Each line represents a $[Cl^-]_i$ measurement along a dendrite in a given frame. Corresponding time points are shown to the right of each trace. NMDA is applied at t = 0 min. **h)** Average ± s.e.m. of MQAE-FLIM $[Cl^-]_i$ readouts across bleb edges reveal a sharp decrease $[Cl^-]_i$ in from bleb to no bleb that occurs over less than a 1 µm span. 'n' denotes 22 blebs from 9 cells.

NMDA induced a rapid increase in *MQAE*-$[Cl^-]_i$ followed by characteristic dendritic blebbing (Fig 6a,b) in depolarized neurons. We observed a surprising, heterogeneous distribution of $[Cl^-]_i$ in excitotoxic conditions, with higher $[Cl^-]_i$ constrained to dendrites that formed blebs (Fig 6c-e). Indeed, $[Cl^-]_i$ in blebs was significantly higher than adjacent dendrites that did not bleb, often reaching peak concentrations of ~80 mM (Fig 6d,e). Pixel-to-pixel lifetime measurements showed that Cl^- microdomains were spatially restricted across the length of dendrites (Fig 6f,g). We resolved precipitous drops in $[Cl^-]_i$ spanning a measured bleb edge length of <1 µm (mean $[Cl^-]_i$ decrease = -26.32±7.9 mM/µm)(Fig 6h), suggesting that the mobility of Cl^- ions is constrained during blebbing.

Excitotoxic Cl^- dysregulation in dendrites is KCC2-dependent

The mechanistic underpinnings of Cl^- entry in dendritic blebbing is a point of contention. Previous work has identified roles for VRACs in cultured neurons *in vitro*, and KCCs and

bioRxiv preprint doi: https://doi.org/10.1101/2020.06.08.139592; this version posted June 9, 2020. The copyright holder for this preprint (which was not certified by peer review) is the author/funder, who has granted bioRxiv a license to display the preprint in perpetuity. It is made available under aCC-BY 4.0 International license.

422 $GABA_A$ receptors in acute brain slices (Allen et al., 2004; Inoue and Okada, 2007; Pond et al.,
423 2006; Steffensen et al., 2015). We sought to dissect which Cl^- transporter or channel activity
424 engendered the abnormally high but discrete $[Cl^-]_i$ accumulations in dendritic blebs. We first
425 confirmed the critical role for Cl^- entry in swelling by reducing extracellular Cl^- from 136.5 mM
426 to 18.5 mM (low$[Cl^-]_o$). Low$[Cl^-]_o$ blocked the Cl^- influx as well as blebbing (Fig 7a-d) down to
427 control levels (+30 mV only group, Fig 7d). Swelling also requires Na^+-influx to drive Cl^- entry
428 and satisfy Gibbs-Donnan equilibrium (Glykys et al., 2017). Consistent with this, reducing Na^+
429 in otherwise normal ACSF decreased NMDA-induced Cl^- influx (Fig 7a-d) and blebbing,
430 confirming that concurrent Na^+ and Cl^- loading is required.

431 We tested the role for NKCC1 in mediating Cl^- entry in swelling by pre-incubating
432 bumetanide prior to NMDA application. Interestingly, bumetanide increased the rate of Cl^-
433 loading during the initial NMDA application but the peak $[Cl^-]_i$ accumulations during the plateau
434 were not different from NMDA alone (Fig 7b,c). In contrast, blocking KCC2 with furosemide
435 dramatically reduced the Cl^- loading rate and average $[Cl^-]_i$ load (Fig 7a-d). Cl^- channel
436 inhibitors, such as 5-Nitro-2-(3-phenylpropylamino)benzoic acid (NPPB, 100 µM) to block
437 VRACs, picrotoxin (100 µM) for $GABA_A$ receptors, and niflumic acid (NFA, 100 µM) to block
438 Ca^{2+} activated Cl^- channels had no effect on NMDA-induced Cl^- loading. Together, these data
439 highlight the importance of the local regulation of Cl- microdomains to maintain dendrite
440 volume. Further, our findings suggest that Cl^- dysregulation in excitotoxic blebbing occurs
441 principally through reversed uptake by KCC2.

442

443

bioRxiv preprint doi: https://doi.org/10.1101/2020.06.08.139592; this version posted June 9, 2020. The copyright holder for this preprint (which was not certified by peer review) is the author/funder, who has granted bioRxiv a license to display the preprint in perpetuity. It is made available under aCC-BY 4.0 International license.

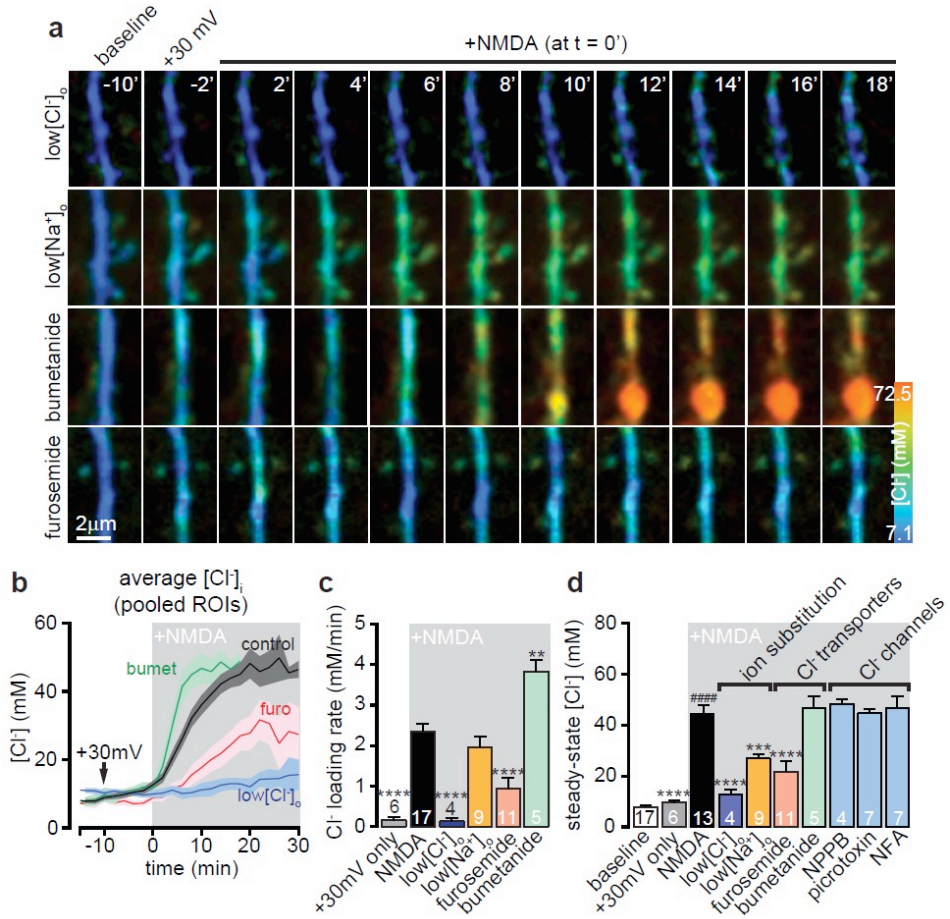

Figure 7. NMDA-induced Cl^- influx and blebbing is KCC2 dependent. a) Example MQAE-FLIM time-lapses of NMDA-induced blebbing in low$[Cl^-]_o$, low$[Na^+]_o$, bumetanide, and furosemide conditions. NMDA (20 µM) was continually applied at time = 0 min. **b)** Average *MQAE*-$[Cl^-]_i$ readouts over time for datasets outlined in 'a'. Data are pooled ROI averages (i.e. encompassing blebbed and non-blebbed ROIs). **c)** Average Cl^- loading rate, calculated from the rising slope of NMDA-induced Cl^- increase from 'b'. +30 mV only indicates continuous depolarization for 40 min. ****P<0.0001 for NMDA alone compared to +30mV, $[Cl^-]_o$, and furosemide conditions, **P = 0.0032 compared to bumetanide, one-way ANOVA with Tukey test. **d)** Quantitative summary of steady-state *MQAE*-$[Cl^-]_i$ at 15 min post NMDA application. ####P<0.0001 NMDA alone vs baseline, ****P<0.0001 significance vs NMDA alone, one-way ANOVA with Tukey test.

bioRxiv preprint doi: https://doi.org/10.1101/2020.06.08.139592; this version posted June 9, 2020. The copyright holder for this preprint (which was not certified by peer review) is the author/funder, who has granted bioRxiv a license to display the preprint in perpetuity. It is made available under aCC-BY 4.0 International license.

Legends for movies 1, 2 and 3 that provide time lapse illustrations for data in Figure 7:

Movie 1: NMDA triggers dendritic [Cl–]i loading and blebbing. Time lapse of MQAE-FLIM images to measure spatiotemporal changes in dendritic [Cl–]i. NMDA (20 µm) application occurs at '+NMDA' tag and is immediately followed by dramatic and localized increases in $[Cl–]_i$ that form dendritic blebs.

Movie 2: Dendritic blebbing requires Cl– influx. Application of NMDA (20 µm) does not generate substantial subcellular increases in low [Cl–]o conditions and dendritic blebbing does not occur, indicating that dendritic NMDA-induced blebbing requires Cl– influx.

Movie 3: Blocking KCC2 with furosemide reduces NMDA-induced Cl– influx and blebbing. Bath pre-application of furosemide (200 µM) dramatically reduced Cl– loading and blebbing in the presence of NMDA (20 µm), indicating that KCC2 transport direction is reversed in cytotoxic edema.

bioRxiv preprint doi: https://doi.org/10.1101/2020.06.08.139592; this version posted June 9, 2020. The copyright holder for this preprint (which was not certified by peer review) is the author/funder, who has granted bioRxiv a license to display the preprint in perpetuity. It is made available under aCC-BY 4.0 International license.

Discussion

Early observations of subcellular $[Cl^-]_i$ heterogeneities using electrophysiology (Alger and Nicoll, 1979; Barker and Ransom, 1978; Nicoll et al., 1976) have been corroborated by recent studies employing ratiometric sensors (Berglund et al., 2006; Glykys et al., 2014; Kuner and Augustine, 2000; Sulis Sato et al., 2017), however our understanding of the spatial regulation and functional impact of these microdomains is limited. Here we demonstrate that pairing MQAE-FLIM with electrophysiology allowed us to provide the first high resolution quantitative measurements of the spatiotemporal $[Cl^-]_i$ dynamics throughout cortical pyramidal dendrites. MQAE-FLIM had both the sensitivity and dynamic range to measure equilibrative $[Cl^-]_i$ changes under resting conditions and cytotoxic changes during intense NMDA receptor stimulation. We quantified the basal contributions of NKCC1 and KCC2 in maintaining $[Cl^-]_i$ at rest as well as modest changes in dendritic $[Cl^-]_i$ incurred by membrane depolarization. Importantly, we report that NMDA-induced cytotoxic swelling is driven by Cl^- influx via KCC2 reversed transport. Our observations lead to the surprising conclusion that discrete microdomains of high $[Cl^-]_i$ can be generated with sharp boundaries that give rise to dendritic blebbing.

Quantifying dendritic Cl^- dynamics and spatial distributions have been longstanding challenges. This is due to the robust homeostatic control of Cl^- gradients, as well as the bidirectional nature of Cl^- flux that depends on dynamic E_m and E_{Cl-} values (Arosio and Ratto, 2014). Additionally Cl^- imaging using many genetically encoded fluorescent proteins is problematic due to pH sensitivity, but also non-uniform distortions caused by the optical properties of brain tissue that alter even ratiometric excitation and emission values (Oheim et al., 2001; Sulis Sato et al., 2017). This is further complicated by volume changes that occur in parallel with $[Cl^-]_i$, which can affect intrinsic optical properties of the tissue and thereby

bioRxiv preprint doi: https://doi.org/10.1101/2020.06.08.139592; this version posted June 9, 2020. The copyright holder for this preprint (which was not certified by peer review) is the author/funder, who has granted bioRxiv a license to display the preprint in perpetuity. It is made available under aCC-BY 4.0 International license.

subsequent intensity changes. Two recent studies show substantial improvements in this area using dual ratiometric Cl^--pH sensors such as ClopHensorN and LSSmClopHesnsor (Mukhtarov et al., 2013; Sulis Sato et al., 2017). However MQAE-FLIM is still preferable for quantitative studies due to its high Cl^- affinity, fast detection kinetics, insensitivity to changes in emission intensity, dye concentration, photobleaching, and light scattering (Arosio and Ratto, 2014; Fukuda et al., 1998; Kovalchuk and Garaschuk, 2012; Marandi et al., 2002; Verkman et al., 1989). MQAE is also relatively insensitive to pH fluctuations (Koncz and Daugirdas, 1994) and viscosity (Kaneko et al., 2002). In support of this, we observed a near-complete inhibition of NMDA-induced rises in *MQAE*-$[Cl^-]_i$ in low$[Cl^-]_o$, even though NMDA triggers cytosolic acidification (Canzoniero et al., 1996). One limitation for imaging MQAE is nonspecific but modest quenching by gluconate, EGTA and HEPES (but notably not by endogenous anions such as SO_4^{2-}, HCO_3^-, and PO_4^{3-}) (Kaneko et al., 2002; Kovalchuk and Garaschuk, 2012). This is typically controlled for by calibrating the dye *in situ*, although complete $[Cl^-]_i$:$[Cl^-]_o$ equilibration is difficult to achieve. Indeed, our measured K_{SV} for *in situ* (6.53 M^{-1}) and *in vitro* (20.19 M^{-1}) calibrations were both within the range of *in situ* experiments from another group (5-20 M^{-1})(Kaneko et al., 2004) and well below MQAE in distilled water (185 M^{-1}). It is therefore beneficial to patch load MQAE, as these unspecific anion interactions can be controlled for by their inclusion in calibration solutions.

Notwithstanding the challenges and considerations associated with lifetime imaging, our MQAE-FLIM readouts from bulk- and pipette-loaded configurations are in agreement with each other and with basal $[Cl^-]_i$ values predicted in the literature (Delpire and Staley, 2014; Kuner and Augustine, 2000; Staley and Proctor, 1999). An important validation of our approach is its accuracy compared to regional E_{GABA} measures. *MQAE*-$[Cl^-]_i$ readouts were <10 mM below

bioRxiv preprint doi: https://doi.org/10.1101/2020.06.08.139592; this version posted June 9, 2020. The copyright holder for this preprint (which was not certified by peer review) is the author/funder, who has granted bioRxiv a license to display the preprint in perpetuity. It is made available under aCC-BY 4.0 International license.

524 E_{GABA}-$[Cl^-]_i$, which we attribute to a combination of $GABA_AR$ HCO_3^- efflux (Kaila, 1994) and
525 imperfect voltage clamp due to K^+ leak in the absence of K^+ channel blockers. Nevertheless, the
526 variance in both our *MQAE*-$[Cl^-]_i$ and E_{GABA}-$[Cl^-]_i$ values were strongly correlated, and
527 commensurate with the physiological heterogeneity in $[Cl^-]_i$ reported by other groups (Barker
528 and Ransom, 1978; Delpire and Staley, 2014; Glykys et al., 2014; Khirug et al., 2008; Kuner and
529 Augustine, 2000; Sulis Sato et al., 2017). There was also no detectable impact of Br^- ion flux
530 either *MQAE*-$[Cl^-]_i$, meaning MQAE-Br could be used over a broad concentration range
531 depending on experimental requirements. The stability of *MQAE*-$[Cl^-]_i$ over a 60 min recording
532 indicates that quenching from endogenous and exogenously (pipette) supplied anion species was
533 minimal relative to Cl^-. Thus, the variability of $[Cl^-]_i$ we observe within neuronal dendrites
534 highlights the clear need for quantitative evaluations of the functional implications of Cl^-
535 microdomains.

536 The temporal dynamics of Cl^- handling has been shown to be modified over time scales
537 of days (during development), minutes (KCC2 posttranslational regulation by calpains or
538 WNK/SPAK), and milliseconds-seconds (ionic plasticity, shunting) (Alessi et al., 2014; Doyon
539 et al., 2016; Kaila et al., 2014). With MQAE-FLIM we quantified transport capacity of NKCC1
540 and KCC2 over time but also at multiple subcellular sites. For example, patched neurons and
541 astrocytes defended their respective low (<10 mM) and high (15-20 mM) $[Cl^-]_i$ setpoints when
542 dialyzed with mismatched Cl^- loads. Interestingly, we observed regional variance in Cl^- export
543 in both cell types, with higher transport efficiency in dendrites and fine processes. MQAE-FLIM
544 also enabled us to measure a wide range of $[Cl^-]_i$ changes. By blocking KCC2 or NKCC1 in
545 dendrites with either furosemide or bumetanide, we could quantify subtle (<5 mM) changes in
546 Cl^- transport at rest with basal synaptic transmission intact. Detection of such modest $[Cl^-]_i$

bioRxiv preprint doi: https://doi.org/10.1101/2020.06.08.139592; this version posted June 9, 2020. The copyright holder for this preprint (which was not certified by peer review) is the author/funder, who has granted bioRxiv a license to display the preprint in perpetuity. It is made available under aCC-BY 4.0 International license.

variations is testament to the sensitivity and practicability of MQAE-FLIM, as millimolar changes would affect excitability (Doyon et al., 2016). We also measured large $[Cl^-]_i$ changes in neurons loaded with $[Cl^-]_{pipette}$ = 80 mM, where somatic and dendritic was reduced typically below 40 mM in part by export via KCC2. This allowed us to also quantify the impact of KCC2 dephosphorylation in T906A/T1007A mice (Friedel et al., 2015; Heubl et al., 2017; Moore et al., 2018; Pisella et al., 2019; Watanabe et al., 2019), where $[Cl^-]_i$ was maintained at near-control levels despite an elevated $[Cl^-]_{pipette}$ load (80 mM). Indeed, there is growing appreciation for dynamic KCC2 phosphorylation, for example in establishing excitatory GABAergic tone during development, impacting cognitive function, and susceptibility to epileptiform activity (Friedel et al., 2015; Moore et al., 2019; Moore et al., 2018; Pisella et al., 2019; Silayeva et al., 2015; Watanabe et al., 2019).

Evidence of spatial $[Cl^-]_i$ heterogeneity within cellular subcompartments in previous studies (Barker and Ransom, 1978; Berglund et al., 2006; Glykys et al., 2014; Khirug et al., 2008; Kuner and Augustine, 2000) suggested that standing Cl^- gradients could exist within cytoplasmic domains of neurons. Our observations of inhomogeneous $[Cl^-]_i$ distributions in dendrites at rest and the dramatic induction of discrete $[Cl^-]_i$ microdomains that lead to dendritic blebs with distinct edges indicates that Cl^- mobility can be spatially restricted. Although controversial (Kaila et al., 2014), the suggestion that Cl^- ions are diffusion-limited, even at rest, has been proposed to occur due to a nonuniform distribution of immobile intracellular and extracellular anions [(Glykys et al., 2014) see also co-submission by Rahmati et al., 2020]. While our data cannot confirm the role of immobile anions in setting Cl^- microdomains, the uneven distribution cytosolic proteins (Gut et al., 2018) could give rise to compensatory heterogeneities in mobile Cl^- ions. In cytotoxic edema, breakdown of negatively charged proteins and structural

bioRxiv preprint doi: https://doi.org/10.1101/2020.06.08.139592; this version posted June 9, 2020. The copyright holder for this preprint (which was not certified by peer review) is the author/funder, who has granted bioRxiv a license to display the preprint in perpetuity. It is made available under aCC-BY 4.0 International license.

actin is well established in excitotoxicity (Halpain et al., 1998; Lipton, 1999) and would likely affect Cl^- mobility in dendrites (Glykys et al., 2014). The possibility of Cl^- microdomains might be expected in some dendritic regions given that dendritic morphology alone can affect ion diffusion. For instance, the thin necks of synaptic spines can restrict Ca^{2+} diffusion and propagation of electrical potentials between spine heads and dendrites (Kwon et al., 2017; Yuste and Denk, 1995). Additionally, recent modelling studies predict that longitudinal Cl^- diffusion in dendrites is restricted by the distribution and strength of K^+-Cl^- cotransporters (Doyon et al., 2011), by tortuosity imposed spines (Mohapatra et al., 2016), and even by passive membrane properties (Lombardi et al., 2019), all of which could affect local GABAergic inhibition and ionic plasticity. Given that little is known about Cl^- microdomains and their regulation at the sub-dendritic level, future studies using MQAE-FLIM will be fundamental to understanding KCC2's vital role in synaptic physiology.

The data presented here indicate that formation of pathological blebs requires reversed KCC2 transport that generates microdomains of high dendritic $[Cl^-]_i$. Quantitative readouts of dendritic $[Cl^-]_i$ revealed spatially discrete increases in Cl^- that were blocked by furosemide, leading to our conclusion that KCC2 drives Cl^- import into blebs. We also observed a surprising increase in Cl^- loading rate when NKCC1 was blocked with bumetanide, indicating that NKCC1 was also pumping in reverse mode (i.e. Cl^- export) which has been suggested to occur when Na^+, K^+, and Cl^- concentration gradients are dramatically altered (Brumback and Staley, 2008; Glykys et al., 2017; Kaila et al., 2014). KCC2 transport direction depends on the outwardly-directed K+ gradient but also the stoichiometry of K^+:Cl^- ions (Payne, 1997). *In silico* and *in vitro* experiments on KCC2 thermodynamic driving force have shown K^+/Cl^- cotransport can reverse when $[K^+]_o$ increases beyond 5 mM (DeFazio et al., 2000; Payne, 1997). Reversed transport is

bioRxiv preprint doi: https://doi.org/10.1101/2020.06.08.139592; this version posted June 9, 2020. The copyright holder for this preprint (which was not certified by peer review) is the author/funder, who has granted bioRxiv a license to display the preprint in perpetuity. It is made available under aCC-BY 4.0 International license.

593 therefore likely to occur in excitoxicity/stroke, where $[K^+]_o$ increases to >60 mM (Hansen and
594 Nedergaard, 1988; Rossi et al., 2007). A recent study showed that brief ischemia induced
595 prolonged (>1hr) increases in neuronal $[Cl^-]_i$ and epileptiform activity that were sensitive to
596 furosemide block (Blauwblomme et al., 2018). Further, the frequently observed decrease in
597 KCC2 expression in neurotraumas (Coull et al., 2003; Jaenisch et al., 2010; Kaila et al., 2014;
598 Zhou et al., 2012) could be explained by the present findings as a protective adaptation to
599 minimize pathological Cl^- loading in neurons. In conclusion, our joint MQAE-FLIM and
600 electrophysiology approach has provided valuable insights into the tight spatiotemporal
601 regulation of $[Cl^-]_i$ microdomains as it relates to integration of synaptic currents, but also in
602 neuropathologies where perturbed Cl^- handling can degrade inhibitory tone in epilepsy or trigger
603 dendritic swelling in cerebral edema (Cohen et al., 2002; Rungta et al., 2015).

604

605 **Methods**

606 **Animals**

607 All animal care protocols were approved by the University of British Columbia's Animal
608 Care Committee in accordance with the Canadian Council on Animal Care guidelines. Acute
609 slice experiments from rat were performed on postnatal day (P) >25 Sprague Dawley rats
610 (Charles River). Mouse experiments were performed on P>25 $KCC2^{AA}$ (homozygous) or
611 $KCC2^{WT}$ animals. All animals were housed on a 12/12hr light/dark cycle with at least one cage
612 mate and *ad libidum* access to laboratory chow and water.

613 **Acute Cortical Slice Preparation**

bioRxiv preprint doi: https://doi.org/10.1101/2020.06.08.139592; this version posted June 9, 2020. The copyright holder for this preprint (which was not certified by peer review) is the author/funder, who has granted bioRxiv a license to display the preprint in perpetuity. It is made available under aCC-BY 4.0 International license.

Rats were anaesthetized by isoflourane inhalation in air and decapitated. The brain was quickly extracted, blocked, and mounted on a vibrating slicer (Leica VT1200S) while submerged in an ice-cold solution consisting of (in mM): 120 NMDG, 2.5 KCl, 25 $NaHCO_3$, 1 $CaCl_2$, 7 $MgCl_2$, 1.25 NaH_2PO_4, 20 glucose, 2.4 Na-pyruvate, 1.3 Na-ascorbate and saturated with 95% O_2/5% CO_2. Transverse cortical slices were cut (370 µm) and transferred into a chamber containing artificial cerebral spinal fluid (aCSF) at 33°C for at least one hour prior to experimentation. aCSF consisted of 126 mM NaCl, 26 mM $NaHCO_3$, 2.5 mM KCl, 1.25 mM NaH_2PO_4, 2 mM $MgCl_2$, 2 mM $CaCl_2$, and 10 mM glucose and was continuously bubbled with 95% O_2/5% CO_2.

Chemicals and Reagents

Drugs and dyes used for experiments are listed in final concentration (in mM) and were purchased from the following suppliers: 0.2 furosemide, 0.1 niflumic acid (Cayman Chemicals), 0.05 bumetanide, 0.05 picrotoxin, 0.02 NMDA, 0.01 tributyltin, all salts for aCSF and slicing solution (Sigma-Aldrich), 0.01 Glycine (EMD Chemicals), 0.1 NPPB, 0.05 bumetanide, and 0.01 nigericin (Tocris), 0.05 Alexa-594 hydrazide, 0.6-8 MQAE (Thermo Fisher Scientific). All drugs were made into aliquots dissolved in water or DMSO and diluted to the final concentration in aCSF or intracellular recording solution – the final concentration of DMSO never exceeded 0.1%.

Electrophysiology

After stabilization, slices were carefully transferred to a recording chamber continually perfused with aCSF (33°C, stage heater from Luigs & Neumann) at a rate of 1-2 mL/min. Layer 4/5 pyramidal neurons in the cortex were identified using widefield infrared (IR) illumination

bioRxiv preprint doi: https://doi.org/10.1101/2020.06.08.139592; this version posted June 9, 2020. The copyright holder for this preprint (which was not certified by peer review) is the author/funder, who has granted bioRxiv a license to display the preprint in perpetuity. It is made available under aCC-BY 4.0 International license.

and captured with an IR-1000 (DAGE-MTI) camera fitted on a LSM 7MP 2-photon imaging system (Zeiss). Whole-cell patch clamp recordings were obtained using thin-walled borosilicate glass microelectrodes (Warner) pulled to a tip resistance of 3-5 MΩ pulled using a P-97 Flaming/Brown Micropipette Puller (Sutter Instrument). Electrodes were filled with an intracellular recording solution containing (in mM): 108 K-Gluconate, 3 KCl, 2 $MgCl_2$, 8 Na-Gluconate, 1 K_2-EGTA, 0.23 $CaCl_2$, 0.05 Alexa-594, 6-8 MQAE, 4 K_2-ATP and 0.3 Na_3-GTP at pH 7.25 with 10 HEPES. 15 minutes was allotted for intracellular equilibration for all experiments unless otherwise indicated. Recordings were made using a MultiClamp 700B amplifier and Digidata 1440A digitiser (Axon Instruments, Molecular Devices) controlled via Clampex 10.7 acquisition software. Cells were voltage clamped at -60 mV unless specified otherwise. Access resistance was always <20 MΩ, and cells with holding currents below -100 pA after break-in were discarded.

Time-Resolved 2-photon fluorescent lifetime imaging setup

All experiments were performed on a LSM 7MP 2-photon imaging system from Zeiss fitted with a SPC-150 FLIM acquisition module from Becker & Hickl. Femtosecond excitation was achieved with a Ti:Sapphire Chameleon Ultra II 2-photon laser (Coherent) pulsing at 80MHz and tuned to 750nm. Laser pulse timing was collected directly from the laser's internal photodiode. Images were acquired with a Zeiss 20X-W/1.0 NA objective at digital zooms ranging from 3x-12x at 256x256 or 128x128 pixel resolutions depending on zoom factor. Emission light was first passed through an IR filter (700nm shortpass) to block spurious excitation light, then split with a 480nm longpass dichroic mirror (Chroma tech). Blue MQAE fluorescence was then filtered with a 460/50nm bandpass filter and collected with a GaAsP hybrid detector (HPM-100-40 hybrid PMT, Becker and Hickl). After the 480nm beam splitter,

bioRxiv preprint doi: https://doi.org/10.1101/2020.06.08.139592; this version posted June 9, 2020. The copyright holder for this preprint (which was not certified by peer review) is the author/funder, who has granted bioRxiv a license to display the preprint in perpetuity. It is made available under aCC-BY 4.0 International license.

red emission from Alexa-594 was passed through a 630/75nm bandpass filter (Chroma) before detection with a LSM BiG GaAsP photomultiplier (Zeiss).

MQAE-FLIM Calibrations

In situ calibrations were conducted as previously described (Gensch et al., 2015; Kovalchuk and Garaschuk, 2012) to measure $[Cl^-]_i$ in neurons and astrocytes bulk loaded with MQAE. Briefly, acute transverse hippocampal/cortical slices were incubated in 6 mM MQAE for 20 min at 33-34°C. Slices were then transferred to the imaging chamber containing the Cl^-/OH^- antiporter tributyltin and the K^+/H^+ ionophore nigericin in a 0-40 mM KCl solution also containing 10 mM HEPES, 10 mM Na-Gluconate, pH balanced to 7.35 with KOH, osmolarity adjusted to 300 with K-Gluconate, and warmed to 33°C.

In vitro MQAE calibrations were performed to match the recording conditions in whole-cell patch clamp experiments. Calibration solutions exactly mimicked the internal recording solution (see '*Electrophysiology*') including Alexa-594. The desired Cl^- concentration was achieved by adjusting the concentration of KCl and was balanced by equimolar K-gluconate. For 2.5mM [Cl^-], some $MgCl_2$ was substituted with $MgSO_4$, as MQAE fluorescence is not quenched by SO_4^{2-} anions (Kaneko et al., 2002). The calibration solution was placed in a sealed micropipette and imaged in warmed (33°C) aCSF under the microscope using consistent experimental parameters as *in situ*. Calibration data were fit in GraphPad Prism 6 with a one-phase exponential decay curve to match the monoexponential decay parameters of MQAE lifetime:

$$Y = (Y_o - A)e^{-K*X} + A$$

bioRxiv preprint doi: https://doi.org/10.1101/2020.06.08.139592; this version posted June 9, 2020. The copyright holder for this preprint (which was not certified by peer review) is the author/funder, who has granted bioRxiv a license to display the preprint in perpetuity. It is made available under aCC-BY 4.0 International license.

Where Y = measured lifetime (in ps), X = $[Cl^-]$, Y_o = lifetime at 0$[Cl^-]$ (in ps), A = lifetime horizontal asymptote at high $[Cl^-]$ (in ps), K = rate constant. Our best-fit line calculated from pooled averages was:

$$Y = (4139 - 1247)e^{-0.02902*X} + 1247$$

Due to the limitations of the curve fit, any measured lifetime values that were above the upper limit of 4139 ps were set to 0 mM $[Cl^-]$. The K_d value for Cl^--dependent MQAE quenching was calculated as K_d=0.69/K.

Fluorescent Lifetime Imaging and Data Analysis

For bulk loaded imaging, slices were loaded with MQAE (6 mM) as described above. Neuronal somata were identified visually, and astrocytes were identified by SR101 stain (1 µM, post-slice incubation) or visually in unstained tissue. Images were acquired by continual XY frame scanning over 15s-60s to ensure adequate photon counts for accurate lifetime curve-fitting at low laser power. All cells were imaged between 50-100µm below the slice surface to balance minimal fluorescent scattering and maximal cell viability. For patch loaded imaging, cells were dialyzed with internal solution containing 6 mM MQAE for a least 15 min prior to imaging to allow for complete equilibration of dye and pipette salts.

Lifetime data were collected in parallel to signal intensity for each pixel and analysed, and the intensity data were used to process lifetime data and for illustration purposes. Lifetime data were processed using SPCImage 7.3 software from Becker & Hickl and decay values of each pixel were calculated based on a monoexponential fit described above. A bin factor of 1 was used to attain a photon count ≥10 at the tail (9ns after laser pulse) and a χ^2 fit value close to 1. Lifetime

bioRxiv preprint doi: https://doi.org/10.1101/2020.06.08.139592; this version posted June 9, 2020. The copyright holder for this preprint (which was not certified by peer review) is the author/funder, who has granted bioRxiv a license to display the preprint in perpetuity. It is made available under aCC-BY 4.0 International license.

decay matrices were decimated from 32 bit to 16 bit by rounding values to the nearest 1 ps in MATLAB (Mathworks). Intensity images were used as a registration template to align the lifetime images in MATLAB, and dendritic lifetime signals were measured in ImageJ. For dendritic recordings, ROIs were mapped on intensity images to ensure signal measurements were in-focus and transferred to the lifetime image. All colour-coded example FLIM images in the figures are intensity-weighted RGB images for ease of visualisation of MQAE signal over background fluorescence.

Rubi-GABA uncaging

Rubi-GABA (Rial Verde et al., 2008) was purchased from Tocris and dissolved directly into recording aCSF at 0.5 mM and stored as frozen aliquots prior to use. The Rubi-GABA solution was always protected from ambient light, during preparation and experimentation. Rubi-GABA was locally puff-ejected near the patched neuron (~100 µm) and held at a constant pressure of 1 psi throughout the experiment. Somatic MQAE-FLIM measures were then taken with the 2-photon laser tuned to 750 nm and imaged at low power (<4 mW) to prevent GABA uncaging during the acquisition. The laser was then tuned to 800 nm for Rubi-GABA photolysis, and uncaging laser power was slowly increased until reliable $GABA_A$ receptor currents were observed at V_m = -80 mV (50 ms pulses). Patched neurons were filled with 8 mM MQAE in 80 mM Cl^- intracellular recording solution, and 0.5 µM TTX was included in normal aCSF to block voltage-gated Na^+ channels. A liquid junction potential of 6 mV was applied to all voltage steps. E_{GABA}-$[Cl^-]_i$ was calculated from E_{GABA} using the Nernst Equation.

Dendritic blebbing assay

bioRxiv preprint doi: https://doi.org/10.1101/2020.06.08.139592; this version posted June 9, 2020. The copyright holder for this preprint (which was not certified by peer review) is the author/funder, who has granted bioRxiv a license to display the preprint in perpetuity. It is made available under aCC-BY 4.0 International license.

To isolate swelling in a single cell we used a high Mg^{2+} (6 mM) aCSF solution to increase the likelihood of voltage-dependent Mg^{2+} block of tissue-wide NMDA receptors as previously described (Dissing-Olesen et al., 2014). Layer 4/5 cortical neurons were whole-cell patch clamped with MQAE in a K-gluconate internal solution described above and held at V_m = -60 mV. Cells were dialyzed for a 10-20 min baseline period prior to imaging, followed by a 10 min depolarization to V_m = +30 mV to ensure complete unblock NMDA receptors in dendrites and accommodate loss of membrane potential control from space clamp issues. Sustained bath application of 20 µM NMDA and 10 µM glycine was used to trigger Cl^- loading and swelling. Low $[Cl^-]_o$ aCSF was made my replacing NaCl with equimolar Na-Gluconate, and low $[Na^+]_o$ aCSF by replacing NaCl with $NMDG^+$ and pH balanced with HCl. Apical dendrites were selected for imaging based on their proximity to the soma for voltage clamp (<100 µm), and images were acquired over 20-30s, typically 160 frames, every 2 min to minimize phototoxicity.

Acknowledgements

N.L.W collected and analyzed the data and wrote and edited the manuscript with B.A.M. N.L.W and K.K. designed the study with B.A.M., and B.A.M. supervised the study.

References

Alessi, D.R., Zhang, J., Khanna, A., Hochdorfer, T., Shang, Y., and Kahle, K.T. (2014). The WNK-SPAK/OSR1 pathway: master regulator of cation-chloride cotransporters. Sci Signal *7*, re3.

Alger, B.E., and Nicoll, R.A. (1979). GABA-mediated biphasic inhibitory responses in hippocampus. Nature *281*, 315-317.

Allen, N.J., Rossi, D.J., and Attwell, D. (2004). Sequential release of GABA by exocytosis and reversed uptake leads to neuronal swelling in simulated ischemia of hippocampal slices. J Neurosci *24*, 3837-3849.

bioRxiv preprint doi: https://doi.org/10.1101/2020.06.08.139592; this version posted June 9, 2020. The copyright holder for this preprint (which was not certified by peer review) is the author/funder, who has granted bioRxiv a license to display the preprint in perpetuity. It is made available under aCC-BY 4.0 International license.

745 Arosio, D., Garau, G., Ricci, F., Marchetti, L., Bizzarri, R., Nifosi, R., and Beltram, F. (2007).
746 Spectroscopic and structural study of proton and halide ion cooperative binding to gfp. Biophysical
747 journal *93*, 232-244.
748 Arosio, D., and Ratto, G.M. (2014). Twenty years of fluorescence imaging of intracellular chloride.
749 Frontiers in cellular neuroscience *8*, 258.
750 Barker, J.L., and Ransom, B.R. (1978). Amino acid pharmacology of mammalian central neurones grown
751 in tissue culture. J Physiol *280*, 331-354.
752 Berglund, K., Schleich, W., Krieger, P., Loo, L.S., Wang, D., Cant, N.B., Feng, G., Augustine, G.J., and
753 Kuner, T. (2006). Imaging synaptic inhibition in transgenic mice expressing the chloride indicator,
754 Clomeleon. Brain cell biology *35*, 207-228.
755 Blaesse, P., Airaksinen, M.S., Rivera, C., and Kaila, K. (2009). Cation-chloride cotransporters and
756 neuronal function. Neuron *61*, 820-838.
757 Blauwblomme, T., Dzhala, V., and Staley, K. (2018). Transient ischemia facilitates neuronal chloride
758 accumulation and severity of seizures. Annals of clinical and translational neurology *5*, 1048-1061.
759 Bormann, J., Hamill, O.P., and Sakmann, B. (1987). Mechanism of anion permeation through channels
760 gated by glycine and gamma-aminobutyric acid in mouse cultured spinal neurones. J Physiol *385*, 243-
761 286.
762 Brumback, A.C., and Staley, K.J. (2008). Thermodynamic regulation of NKCC1-mediated Cl-
763 cotransport underlies plasticity of GABA(A) signaling in neonatal neurons. J Neurosci *28*, 1301-1312.
764 Canzoniero, L.M., Sensi, S.L., and Choi, D.W. (1996). Recovery from NMDA-induced intracellular
765 acidification is delayed and dependent on extracellular bicarbonate. The American journal of physiology
766 *270*, C593-599.
767 Chen, L.C., Lloyd, W.R., 3rd, Chang, C.W., Sud, D., and Mycek, M.A. (2013). Fluorescence lifetime
768 imaging microscopy for quantitative biological imaging. Methods in cell biology *114*, 457-488.
769 Chevy, Q., Heubl, M., Goutierre, M., Backer, S., Moutkine, I., Eugene, E., Bloch-Gallego, E., Levi, S.,
770 and Poncer, J.C. (2015). KCC2 Gates Activity-Driven AMPA Receptor Traffic through Cofilin
771 Phosphorylation. J Neurosci *35*, 15772-15786.
772 Cohen, I., Navarro, V., Clemenceau, S., Baulac, M., and Miles, R. (2002). On the origin of interictal
773 activity in human temporal lobe epilepsy in vitro. Science *298*, 1418-1421.
774 Cordero-Erausquin, M., Coull, J.A., Boudreau, D., Rolland, M., and De Koninck, Y. (2005). Differential
775 maturation of GABA action and anion reversal potential in spinal lamina I neurons: impact of chloride
776 extrusion capacity. J Neurosci *25*, 9613-9623.
777 Coull, J.A., Boudreau, D., Bachand, K., Prescott, S.A., Nault, F., Sik, A., De Koninck, P., and De
778 Koninck, Y. (2003). Trans-synaptic shift in anion gradient in spinal lamina I neurons as a mechanism of
779 neuropathic pain. Nature *424*, 938-942.
780 DeFazio, R.A., Keros, S., Quick, M.W., and Hablitz, J.J. (2000). Potassium-coupled chloride cotransport
781 controls intracellular chloride in rat neocortical pyramidal neurons. J Neurosci *20*, 8069-8076.
782 Delpire, E., and Staley, K.J. (2014). Novel determinants of the neuronal Cl− concentration. J Physiol *592*,
783 4099-4114.
784 Dissing-Olesen, L., LeDue, J.M., Rungta, R.L., Hefendehl, J.K., Choi, H.B., and MacVicar, B.A. (2014).
785 Activation of neuronal NMDA receptors triggers transient ATP-mediated microglial process outgrowth. J
786 Neurosci *34*, 10511-10527.
787 Doyon, N., Prescott, S.A., Castonguay, A., Godin, A.G., Kroger, H., and De Koninck, Y. (2011). Efficacy
788 of synaptic inhibition depends on multiple, dynamically interacting mechanisms implicated in chloride
789 homeostasis. PLoS computational biology *7*, e1002149.
790 Doyon, N., Vinay, L., Prescott, S.A., and De Koninck, Y. (2016). Chloride Regulation: A Dynamic
791 Equilibrium Crucial for Synaptic Inhibition. Neuron *89*, 1157-1172.
792 Friedel, P., Kahle, K.T., Zhang, J., Hertz, N., Pisella, L.I., Buhler, E., Schaller, F., Duan, J., Khanna,
793 A.R., Bishop, P.N.*, et al.* (2015). WNK1-regulated inhibitory phosphorylation of the KCC2 cotransporter
794 maintains the depolarizing action of GABA in immature neurons. Sci Signal *8*, ra65.

bioRxiv preprint doi: https://doi.org/10.1101/2020.06.08.139592; this version posted June 9, 2020. The copyright holder for this preprint (which was not certified by peer review) is the author/funder, who has granted bioRxiv a license to display the preprint in perpetuity. It is made available under aCC-BY 4.0 International license.

795 Fukuda, A., Tanaka, M., Yamada, Y., Muramatsu, K., Shimano, Y., and Nishino, H. (1998).
796 Simultaneous optical imaging of intracellular Cl- in neurons in different layers of rat neocortical slices:
797 advantages and limitations. Neuroscience research *32*, 363-371.
798 Funk, K., Woitecki, A., Franjic-Wurtz, C., Gensch, T., Mohrlen, F., and Frings, S. (2008). Modulation of
799 chloride homeostasis by inflammatory mediators in dorsal root ganglion neurons. Molecular pain *4*, 32.
800 Garand, D., Mahadevan, V., and Woodin, M.A. (2019). Ionotropic and metabotropic kainate receptor
801 signalling regulates Cl(-) homeostasis and GABAergic inhibition. J Physiol *597*, 1677-1690.
802 Gauvain, G., Chamma, I., Chevy, Q., Cabezas, C., Irinopoulou, T., Bodrug, N., Carnaud, M., Levi, S.,
803 and Poncer, J.C. (2011). The neuronal K-Cl cotransporter KCC2 influences postsynaptic AMPA receptor
804 content and lateral diffusion in dendritic spines. Proc Natl Acad Sci U S A *108*, 15474-15479.
805 Gensch, T., Untiet, V., Franzen, A., Kovermann, P., and Fahlke, C. (2015). Determination of Intracellular
806 Chloride Concentrations by Fluorescence Lifetime Imaging. Advanced Time-Correlated Single Photon
807 Counting Applications *111*, 189-211.
808 Gilbert, D., Franjic-Wurtz, C., Funk, K., Gensch, T., Frings, S., and Mohrlen, F. (2007). Differential
809 maturation of chloride homeostasis in primary afferent neurons of the somatosensory system.
810 International journal of developmental neuroscience : the official journal of the International Society for
811 Developmental Neuroscience *25*, 479-489.
812 Glykys, J., Dzhala, V., Egawa, K., Balena, T., Saponjian, Y., Kuchibhotla, K.V., Bacskai, B.J., Kahle,
813 K.T., Zeuthen, T., and Staley, K.J. (2014). Local impermeant anions establish the neuronal chloride
814 concentration. Science *343*, 670-675.
815 Glykys, J., Dzhala, V., Egawa, K., Kahle, K.T., Delpire, E., and Staley, K. (2017). Chloride
816 Dysregulation, Seizures, and Cerebral Edema: A Relationship with Therapeutic Potential. Trends in
817 neurosciences *40*, 276-294.
818 Grimley, J.S., Li, L., Wang, W., Wen, L., Beese, L.S., Hellinga, H.W., and Augustine, G.J. (2013).
819 Visualization of synaptic inhibition with an optogenetic sensor developed by cell-free protein engineering
820 automation. J Neurosci *33*, 16297-16309.
821 Gulyas, A.I., Sik, A., Payne, J.A., Kaila, K., and Freund, T.F. (2001). The KCl cotransporter, KCC2, is
822 highly expressed in the vicinity of excitatory synapses in the rat hippocampus. The European journal of
823 neuroscience *13*, 2205-2217.
824 Gut, G., Herrmann, M.D., and Pelkmans, L. (2018). Multiplexed protein maps link subcellular
825 organization to cellular states. Science *361*.
826 Halpain, S., Hipolito, A., and Saffer, L. (1998). Regulation of F-Actin Stability in Dendritic Spines by
827 Glutamate Receptors and Calcineurin. The Journal of Neuroscience *18*, 9835-9844.
828 Hansen, A.J., and Nedergaard, M. (1988). Brain ion homeostasis in cerebral ischemia. Neurochemical
829 pathology *9*, 195-209.
830 Heubl, M., Zhang, J., Pressey, J.C., Al Awabdh, S., Renner, M., Gomez-Castro, F., Moutkine, I., Eugene,
831 E., Russeau, M., Kahle, K.T.*, et al.* (2017). GABAA receptor dependent synaptic inhibition rapidly tunes
832 KCC2 activity via the Cl(-)-sensitive WNK1 kinase. Nat Commun *8*, 1776.
833 Hyde, T.M., Lipska, B.K., Ali, T., Mathew, S.V., Law, A.J., Metitiri, O.E., Straub, R.E., Ye, T.,
834 Colantuoni, C., Herman, M.M.*, et al.* (2011). Expression of GABA signaling molecules KCC2, NKCC1,
835 and GAD1 in cortical development and schizophrenia. J Neurosci *31*, 11088-11095.
836 Inoue, H., and Okada, Y. (2007). Roles of volume-sensitive chloride channel in excitotoxic neuronal
837 injury. J Neurosci *27*, 1445-1455.
838 Jaenisch, N., Witte, O.W., and Frahm, C. (2010). Downregulation of potassium chloride cotransporter
839 KCC2 after transient focal cerebral ischemia. Stroke *41*, e151-159.
840 Jun, I., Cheng, M.H., Sim, E., Jung, J., Suh, B.L., Kim, Y., Son, H., Park, K., Kim, C.H., Yoon, J.H.*, et*
841 *al.* (2016). Pore dilatation increases the bicarbonate permeability of CFTR, ANO1 and glycine receptor
842 anion channels. J Physiol *594*, 2929-2955.
843 Kahle, K.T., Deeb, T.Z., Puskarjov, M., Silayeva, L., Liang, B., Kaila, K., and Moss, S.J. (2013).
844 Modulation of neuronal activity by phosphorylation of the K-Cl cotransporter KCC2. Trends in
845 neurosciences *36*, 726-737.

bioRxiv preprint doi: https://doi.org/10.1101/2020.06.08.139592; this version posted June 9, 2020. The copyright holder for this preprint (which was not certified by peer review) is the author/funder, who has granted bioRxiv a license to display the preprint in perpetuity. It is made available under aCC-BY 4.0 International license.

Kaila, K. (1994). Ionic basis of GABAA receptor channel function in the nervous system. Progress in neurobiology *42*, 489-537.
Kaila, K., Price, T.J., Payne, J.A., Puskarjov, M., and Voipio, J. (2014). Cation-chloride cotransporters in neuronal development, plasticity and disease. Nature reviews Neuroscience *15*, 637-654.
Kaila, K., and Voipio, J. (1987). Postsynaptic fall in intracellular pH induced by GABA-activated bicarbonate conductance. Nature *330*, 163-165.
Kaila, K., Voipio, J., Paalasmaa, P., Pasternack, M., and Deisz, R.A. (1993). The role of bicarbonate in GABAA receptor-mediated IPSPs of rat neocortical neurones. J Physiol *464*, 273-289.
Kaneko, H., Putzier, I., Frings, S., and Gensch, T. (2002). Determination of intracellular chloride concentration in dorsal root ganglion neurons by fluorescence lifetime imaging. Current Topics in Membranes *53*, 167-189.
Kaneko, H., Putzier, I., Frings, S., Kaupp, U.B., and Gensch, T. (2004). Chloride accumulation in mammalian olfactory sensory neurons. J Neurosci *24*, 7931-7938.
Kettenmann, H., and Schachner, M. (1985). Pharmacological properties of gamma-aminobutyric acid-, glutamate-, and aspartate-induced depolarizations in cultured astrocytes. J Neurosci *5*, 3295-3301.
Khirug, S., Yamada, J., Afzalov, R., Voipio, J., Khiroug, L., and Kaila, K. (2008). GABAergic depolarization of the axon initial segment in cortical principal neurons is caused by the Na-K-2Cl cotransporter NKCC1. J Neurosci *28*, 4635-4639.
Koncz, C., and Daugirdas, J. (1994). Use of MQAE for measurement of intracellular [Cl-] in cultured aortic smooth muscle cells. American Journal of Physiology *Dec*, H2114-2123.
Kovalchuk, Y., and Garaschuk, O. (2012). Two-photon chloride imaging using MQAE in vitro and in vivo. Cold Spring Harbor protocols *2012*, 778-785.
Kuner, T., and Augustine, G.J. (2000). A genetically encoded ratiometric indicator for chloride: capturing chloride transients in cultured hippocampal neurons. Neuron *27*, 447-459.
Kwon, T., Sakamoto, M., Peterka, D.S., and Yuste, R. (2017). Attenuation of Synaptic Potentials in Dendritic Spines. Cell reports *20*, 1100-1110.
Lipton, P. (1999). Ischemic cell death in brain neurons. Physiol Rev *79*, 1431-1568.
Lloyd, W.R., Wilson, R.H., Chang, C.W., Gillispie, G.D., and Mycek, M.A. (2010). Instrumentation to rapidly acquire fluorescence wavelength-time matrices of biological tissues. Biomed Opt Express *1*, 574-586.
Lombardi, A., Jedlicka, P., Luhmann, H.J., and Kilb, W. (2019). Interactions between Membrane Resistance, GABA-A Receptor Properties, Bicarbonate Dynamics and Cl(-)-Transport Shape Activity-Dependent Changes of Intracellular Cl(-) Concentration. Int J Mol Sci *20*.
MacVicar, B.A., Tse, F.W., Crichton, S.A., and Kettenmann, H. (1989). GABA-activated Cl- channels in astrocytes of hippocampal slices. J Neurosci *9*, 3577-3583.
Marandi, N., Konnerth, A., and Garaschuk, O. (2002). Two-photon chloride imaging in neurons of brain slices. Pflugers Archiv : European journal of physiology *445*, 357-365.
Mohapatra, N., Tonnesen, J., Vlachos, A., Kuner, T., Deller, T., Nagerl, U.V., Santamaria, F., and Jedlicka, P. (2016). Spines slow down dendritic chloride diffusion and affect short-term ionic plasticity of GABAergic inhibition. Sci Rep *6*, 23196.
Moore, Y.E., Conway, L.C., Wobst, H.J., Brandon, N.J., Deeb, T.Z., and Moss, S.J. (2019). Developmental Regulation of KCC2 Phosphorylation Has Long-Term Impacts on Cognitive Function. Frontiers in molecular neuroscience *12*, 173.
Moore, Y.E., Deeb, T.Z., Chadchankar, H., Brandon, N.J., and Moss, S.J. (2018). Potentiating KCC2 activity is sufficient to limit the onset and severity of seizures. Proc Natl Acad Sci U S A *115*, 10166-10171.
Mukhtarov, M., Liguori, L., Waseem, T., Rocca, F., Buldakova, S., Arosio, D., and Bregestovski, P. (2013). Calibration and functional analysis of three genetically encoded Cl(-)/pH sensors. Frontiers in molecular neuroscience *6*, 9.

bioRxiv preprint doi: https://doi.org/10.1101/2020.06.08.139592; this version posted June 9, 2020. The copyright holder for this preprint (which was not certified by peer review) is the author/funder, who has granted bioRxiv a license to display the preprint in perpetuity. It is made available under aCC-BY 4.0 International license.

Murphy, T.H., Li, P., Betts, K., and Liu, R. (2008). Two-photon imaging of stroke onset in vivo reveals that NMDA-receptor independent ischemic depolarization is the major cause of rapid reversible damage to dendrites and spines. J Neurosci *28*, 1756-1772.

Nicoll, R.A., Padjen, A., and Barker, J.L. (1976). Analysis of amino acid responses on frog motoneurones. Neuropharmacology *15*, 45-53.

Oheim, M., Beaurepaire, E., Chaigneau, E., Mertz, J., and Charpak, S. (2001). Two-photon microscopy in brain tissue: parameters influencing the imaging depth. Journal of neuroscience methods *111*, 29-37.

Payne, J.A. (1997). Functional characterization of the neuronal-specific K-Cl cotransporter: implications for [K+]o regulation. The American journal of physiology *273*, C1516-1525.

Pisella, L.I., Gaiarsa, J.L., Diabira, D., Zhang, J., Khalilov, I., Duan, J., Kahle, K.T., and Medina, I. (2019). Impaired regulation of KCC2 phosphorylation leads to neuronal network dysfunction and neurodevelopmental pathology. Sci Signal *12*.

Pond, B.B., Berglund, K., Kuner, T., Feng, G., Augustine, G.J., and Schwartz-Bloom, R.D. (2006). The chloride transporter Na(+)-K(+)-Cl- cotransporter isoform-1 contributes to intracellular chloride increases after in vitro ischemia. J Neurosci *26*, 1396-1406.

Rial Verde, E.M., Zayat, L., Etchenique, R., and Yuste, R. (2008). Photorelease of GABA with Visible Light Using an Inorganic Caging Group. Frontiers in neural circuits *2*, 2.

Rinehart, J., Maksimova, Y.D., Tanis, J.E., Stone, K.L., Hodson, C.A., Zhang, J., Risinger, M., Pan, W., Wu, D., Colangelo, C.M.*, et al.* (2009). Sites of regulated phosphorylation that control K-Cl cotransporter activity. Cell *138*, 525-536.

Rossi, D.J., Brady, J.D., and Mohr, C. (2007). Astrocyte metabolism and signaling during brain ischemia. Nature neuroscience *10*, 1377-1386.

Rothman, S.M. (1985). The neurotoxicity of excitatory amino acids is produced by passive chloride influx. J Neurosci *5*, 1483-1489.

Rungta, R.L., Choi, H.B., Tyson, J.R., Malik, A., Dissing-Olesen, L., Lin, P.J.C., Cain, S.M., Cullis, P.R., Snutch, T.P., and MacVicar, B.A. (2015). The cellular mechanisms of neuronal swelling underlying cytotoxic edema. Cell *161*, 610-621.

Silayeva, L., Deeb, T.Z., Hines, R.M., Kelley, M.R., Munoz, M.B., Lee, H.H., Brandon, N.J., Dunlop, J., Maguire, J., Davies, P.A.*, et al.* (2015). KCC2 activity is critical in limiting the onset and severity of status epilepticus. Proc Natl Acad Sci U S A *112*, 3523-3528.

Staley, K.J., and Proctor, W.R. (1999). Modulation of mammalian dendritic GABA(A) receptor function by the kinetics of Cl- and HCO3- transport. J Physiol *519 Pt 3*, 693-712.

Steffensen, A.B., Sword, J., Croom, D., Kirov, S.A., and MacAulay, N. (2015). Chloride Cotransporters as a Molecular Mechanism underlying Spreading Depolarization-Induced Dendritic Beading. J Neurosci *35*, 12172-12187.

Su, G., Kintner, D.B., Flagella, M., Shull, G.E., and Sun, D. (2002). Astrocytes from Na(+)-K(+)-Cl(-) cotransporter-null mice exhibit absence of swelling and decrease in EAA release. Am J Physiol Cell Physiol *282*, C1147-1160.

Sulis Sato, S., Artoni, P., Landi, S., Cozzolino, O., Parra, R., Pracucci, E., Trovato, F., Szczurkowska, J., Luin, S., Arosio, D.*, et al.* (2017). Simultaneous two-photon imaging of intracellular chloride concentration and pH in mouse pyramidal neurons in vivo. Proc Natl Acad Sci U S A *114*, E8770-E8779.

Tao, R., Li, C., Newburn, E.N., Ye, T., Lipska, B.K., Herman, M.M., Weinberger, D.R., Kleinman, J.E., and Hyde, T.M. (2012). Transcript-specific associations of SLC12A5 (KCC2) in human prefrontal cortex with development, schizophrenia, and affective disorders. J Neurosci *32*, 5216-5222.

Thompson, R.J., Jackson, M.F., Olah, M.E., Rungta, R.L., Hines, D.J., Beazely, M.A., MacDonald, J.F., and MacVicar, B.A. (2008). Activation of pannexin-1 hemichannels augments aberrant bursting in the hippocampus. Science *322*, 1555-1559.

Tsien, R.Y. (1998). The green fluorescent protein. Annual review of biochemistry *67*, 509-544.

Untiet, V., Kovermann, P., Gerkau, N.J., Gensch, T., Rose, C.R., and Fahlke, C. (2017). Glutamate transporter-associated anion channels adjust intracellular chloride concentrations during glial maturation. Glia *65*, 388-400.

bioRxiv preprint doi: https://doi.org/10.1101/2020.06.08.139592; this version posted June 9, 2020. The copyright holder for this preprint (which was not certified by peer review) is the author/funder, who has granted bioRxiv a license to display the preprint in perpetuity. It is made available under aCC-BY 4.0 International license.

946 Untiet, V., Moeller, L.M., Ibarra-Soria, X., Sanchez-Andrade, G., Stricker, M., Neuhaus, E.M., Logan,
947 D.W., Gensch, T., and Spehr, M. (2016). Elevated Cytosolic Cl- Concentrations in Dendritic Knobs of
948 Mouse Vomeronasal Sensory Neurons. Chemical senses *41*, 669-676.
949 Verkman, A.S., Sellers, M.C., Chao, A.C., Leung, T., and Ketcham, R. (1989). Synthesis and
950 characterization of improved chloride-sensitive fluorescent indicators for biological applications.
951 Analytical biochemistry *178*, 355-361.
952 Watanabe, M., Zhang, J., Mansuri, M.S., Duan, J., Karimy, J.K., Delpire, E., Alper, S.L., Lifton, R.P.,
953 Fukuda, A., and Kahle, K.T. (2019). Developmentally regulated KCC2 phosphorylation is essential for
954 dynamic GABA-mediated inhibition and survival. Sci Signal *12*.
955 Weilinger, N.L., Lohman, A.W., Rakai, B.D., Ma, E.M., Bialecki, J., Maslieieva, V., Rilea, T., Bandet,
956 M.V., Ikuta, N.T., Scott, L.*, et al.* (2016). Metabotropic NMDA receptor signaling couples Src family
957 kinases to pannexin-1 during excitotoxicity. Nature neuroscience *19*, 432-442.
958 Weilinger, N.L., Tang, P.L., and Thompson, R.J. (2012). Anoxia-induced NMDA receptor activation
959 opens pannexin channels via Src family kinases. J Neurosci *32*, 12579-12588.
960 Williams, J.R., and Payne, J.A. (2004). Cation transport by the neuronal K(+)-Cl(-) cotransporter KCC2:
961 thermodynamics and kinetics of alternate transport modes. Am J Physiol Cell Physiol *287*, C919-931.
962 Williams, J.R., Sharp, J.W., Kumari, V.G., Wilson, M., and Payne, J.A. (1999). The neuron-specific K-Cl
963 cotransporter, KCC2. Antibody development and initial characterization of the protein. J Biol Chem *274*,
964 12656-12664.
965 Williams, S.R., and Mitchell, S.J. (2008). Direct measurement of somatic voltage clamp errors in central
966 neurons. Nature neuroscience *11*, 790-798.
967 Yuste, R., and Denk, W. (1995). Dendritic spines as basic functional units of neuronal integration. Nature
968 *375*, 682-684.
969 Zhou, H.Y., Chen, S.R., Byun, H.S., Chen, H., Li, L., Han, H.D., Lopez-Berestein, G., Sood, A.K., and
970 Pan, H.L. (2012). N-methyl-D-aspartate receptor- and calpain-mediated proteolytic cleavage of K+-Cl-
971 cotransporter-2 impairs spinal chloride homeostasis in neuropathic pain. J Biol Chem *287*, 33853-33864.

972